1 **Secondary aerosol formation in marine Arctic environments: A model measurement**

2 **comparison at Ny-Ålesund**

3 Carlton Xavier[1], Metin Baykara[1,2], Robin Wollesen de Jonge[3], Barbara Altstädter[4], Petri

4 Clusius[1], Ville Vakkari[5,6], Roseline Thakur[1], Lisa Beck[1], Silvia Becagli[7], Mirko Severi[7], Rita

5 Traversi[7], Radovan Krejci[8,9], Peter Tunved[8,9], Mauro Mazzola[10], Birgit Wehner[11], Mikko

6 Sipilä[1], Markku Kulmala[1], Michael Boy[1,12], Pontus Roldin[3]

7 [1]Institute for Atmospheric and Earth Systems Research, University of Helsinki, P.O. Box 64, 00014 Helsinki,
8 Finland
9 [2]Climate and Marine Sciences Department, Eurasia Institute of Earth Sciences, Istanbul Technical University,
10 Maslak 34469, Istanbul, Turkey
11 [3]Division of Nuclear Physics, Department of Physics, Lund University, P. O. Box 118 SE-221 00 Lund, Sweden
12 [4]Institute of Flight Guidance, Technische Universität Braunschweig, 38108 Braunschweig, Germany
13 [5]Atmospheric Chemistry Research Group, Chemical Resource Beneficiation, North-West University,
14 Potchefstroom, South Africa
15 [6]Finnish Meteorological Institute, POBox 503, FI-00101 Helsinki, Finland
16 [7]Department of Chemistry, University of Florence, Sesto Fiorentino, 50019 Florence, Italy
17 [8]Department of Environmental Science, Stockholm University, Stockholm, Sweden
18 [9]Bolin Centre for Climate Research, Stockholm University, Stockholm, Sweden
19 [10]National Research Council of Italy, Institute of Polar Sciences (CNR-ISP)
20 [11]Institute of Tropospheric Research, 04318 Leipzig, Germany
21 [12]LUT School of Engineering Science, Lappeenranta-Lahti University of Technology, P.O.Box 20, 53851
22 Lappeenranta, Finland

24 **Correspondence:** Carlton Xavier (carlton.xavier@helsinki.fi) and Pontus Roldin
25 (pontus.roldin@nuclear.lu.se)

27 **Abstract**

28 In this study, we modeled the aerosol particle formation along air mass trajectories arriving at

29 the remote Arctic research stations Gruvebadet (67 m a.s.l) and Zeppelin (474 m a.s.l), Ny-

30 Ålesund during May 2018. The aim of this study was to improve our understanding of

31 processes governing secondary aerosol formation in remote Arctic marine environments. We

32 run the Lagrangian chemistry transport model ADCHEM, along air mass trajectories

33 generated with FLEXPART v10.4. The air masses arriving at Ny-Ålesund spent most of their

34 time over the open ice-free ocean. In order to capture the secondary aerosol formation from

35 the DMS emitted by phytoplankton from the ocean surface, we implemented a recently

36 developed comprehensive DMS and halogen multi-phase oxidation chemistry scheme,

37 coupled with the widely used Master Chemical Mechanism (MCM).

38 The modeled median particle number size distributions are in close agreement with the

39 observations in the marine influenced boundary layer at near sea surface Gruvebadet site.

40 However, while the model reproduces the accumulation mode particle number concentrations

at Zeppelin, it overestimates the Aitken mode particle number concentrations by a factor of ~5.5. We attribute this to the deficiency of the model to capture the complex orographic effects on the boundary layer dynamics at Ny-Ålesund. However, the model reproduces the average vertical particle number concentration profiles within the boundary layer (0-600 m a.s.l.) above Gruvebadet, as measured with Condensation Particle Counters (CPCs) on board an Unmanned Aircraft Systems (UAS).

The model successfully reproduces the observed Hoppel minima, often seen in particle number size distributions at Ny-Ålesund. The model also supports the previous experimental findings that ion mediated H_2SO_4-NH_3 nucleation can explain the observed new particle formation in the marine Arctic boundary layer in the vicinity of Ny-Ålesund. Precursors resulting from gas and aqueous phase DMS chemistry contribute to the subsequent growth of the secondary aerosols. The growth of particles is primarily driven via H_2SO_4 condensation and formation of methane sulfonic acid (MSA) through the aqueous-phase ozonolysis of methane sulfinic acid (MSIA) in cloud and deliquescent droplets.

1. Introduction

The Earth's radiation budget is influenced both directly and indirectly by aerosols, which scatter and absorb the incoming short-wave radiation (direct effect) and serve as cloud condensation nuclei (CCN, indirect effect), affecting both short and long-wave radiation (Gantt et al., 2014; Oshima et al., 2020; Park et al., 2017; Scott et al., 2014). The Arctic environments are susceptible to perturbations in the radiation balance, with some estimates suggesting that, compared to the global average, the Arctic is warming at three times the rate, a phenomenon termed as Arctic amplification (AMAP, 2011, 2017, 2021; Lenssen et al., 2019; Tunved et al., 2013). The warming of the Arctic polar environment has accelerated sea ice loss, leading to a rapid decline in the extent and duration of snow cover and increase in permafrost thaw (AMAP, 2011, 2017; Bengtsson et al., 2013).

The Arctic aerosol number concentration shows a pronounced seasonal variation, where the late winter and early spring period is characterized by elevated accumulation mode aerosol concentrations, accompanied by trace gases (mostly anthropogenic with long-range transported trace elements such as sulfates, soot, and Peroxy Acyl Nitrates (PANs)). This annually recurring phenomenon in late winter and spring is termed the Arctic Haze (Barrie, 1986; Lupi et al., 2016; Tunved et al., 2013). This contrasts with the summer period, when the

atmospheric new particle formation is observed at Arctic sites, most likely due to low background aerosol concentrations, increased photo-chemistry and biological activity (Engvall et al., 2008; Heintzenberg et al., 2017; Tunved et al., 2013).

The climate change driven Arctic sea ice loss has a profound impact on natural aerosol production. Arrigo and van Dijken, (2015) found that decreasing and thinning of sea ice increased the rates of phytoplankton net primary production by ~20% between the years 1998 and 2009. This can lead to an increase in the emissions of primary biogenic precursors such as dimethyl sulfide (DMS), nitrogen volatiles (e.g. alkyl-amines) (Dall'Osto et al., 2017a; Dallósto et al., 2017b) and biological iodine species (Cuevas et al., 2018). DMS is emitted into the atmosphere via air-sea gas exchanges (Park et al., 2017; Uhlig et al., 2019), and accounts for ~80% of global natural sulfur emissions (Kettle and Andreae, 2000; Uhlig et al., 2019). Methane sulfonic acid (MSA) and sulphuric acid (H_2SO_4) is formed via DMS gas-phase oxidation by OH and halogen species (Cl, Br) (Hoffmann et al., 2016; Kim et al., 2021; Wollesen de Jonge et al., 2021). MSA and H_2SO_4, together with ammonia (NH_3) or amines, act as precursors contributing to new particle formation (NPF) and subsequently to CCN production, influencing cloud formation and radiative balance (Berndt et al., 2020; Dall'Osto et al., 2017b; Hoffmann et al., 2016; Kim et al., 2021, Jang et al., 2021; Park et al., 2021). NH_3 plays a major role in particle formation through stabilization of sulfuric acid clusters (Beck et al., 2021; Jokinen et al., 2018; Olenius et al., 2013). Depending on local parameters such as ocean pH, salinity and temperature, global oceans can act either as a source or sink of NH_3 (Paulot et al., 2015). Apart from participating in cluster formation, NH_3 influences the pH of marine aerosols by neutralizing the acid (H_2SO_4 and MSA) in the particles (Paulot et al., 2015). Though a few potential sources of NH_3 are known, for example coastal sea bird colonies, pockets of open water and melting sea ice in summertime Arctic, the magnitude of the emissions remain uncertain (Dall'osto et al., 2019a; Riddick et al., 2012; Wentworth et al., 2016).

DMS oxidation chemistry has been under focus, but uncertainties in climate predictions persist since the chemical transport models (CTMs) and global climate models (GCMs) employ fixed MSA and SO_2 yields from gas-phase oxidation of DMS to calculate aerosol formation (Hertel et al., 1994; Hoffmann et al., 2016; Kloster et al., 2006; Wollesen de Jonge et al., 2021). Including a detailed multi-phase (aqueous-phase chemistry coupled with gas-phase chemistry) DMS chemistry in numerical models can overcome these uncertainties (Barnes et al., 2006; Campolongo et al., 1999). Reaction intermediates such as dimethyl sulfoxide (DMSO), dimethyl sulfone ($DMSO_2$), methane sulfinic acid (MSIA) are water-

107 soluble, and experiments have shown that neglecting aqueous phase chemistry leads to either
108 an under-estimation of modeled MSA (Campolongo et al., 1999), or an over-estimation of
109 gaseous SO_2 compared to measured values (Hoffmann et al., 2016). For example, the
110 temperature dependent ratio of MSA/non-sea-salt SO_4^{2-} (nss-SO_4^{2-}) is often used to estimate
111 the contribution of DMS to sulfate budget (Ayers et al., 1999; Barnes et al., 2006).
112 Campolongo et al., 1999 showed that modeling studies which included a multi-phase DMS
113 chemistry can bridge the gap between temperature-dependent observations and modeled
114 MSA/nss-SO_4^{2-}. Incorporating reactive halogens species over marine environments is crucial
115 in determining the DMS oxidation pathways to either SO_2 or MSA, the aging of marine
116 aerosols and the radiative properties of marine clouds (Hoffmann et al., 2016). Modeling
117 studies have shown that Cl^- and BrO^- radicals in the gas phase act as important DMS sinks
118 (Chen et al., 2018; Wollesen de Jonge et al., 2021), further underlining the role of halogen-
119 DMS chemistry in the marine boundary layer.

120 Recent DMS+OH oxidation experiments performed in the AURA chamber at Aarhus
121 University show that MSA dominates the secondary aerosol mass formation (Rosati et al.,
122 2021). Aerosol dynamics model simulations which intended to replicate the observations
123 during these AURA experiments, using the DMS gas-phase chemistry scheme from the
124 Master Chemical Mechanism, MCMv3.3.1, (Jenkin et al., 1997, 2015; Saunders et al., 2003),
125 substantially underestimates the particle mass and number concentrations and the MSA:SO_4^{2-}
126 ratio (Rosati et al., 2021, Wollesen de Jonge, 2021). Based on these findings, Wollesen de
127 Jonge et al. (2021) developed a new DMS multi-phase chemistry scheme based on MCM
128 v3.3.1, CAPRAM DMS module 1.0 (DM1.0) (Hoffmann et al., 2016), a subset of the multi-
129 phase halogen chemistry mechanism CAPRAM Halogen Module 2.0 (HM2.0) (Bräuer et al.,
130 2013) and new reactions leading to the formation of hydroperoxymethyl thioformate
131 (HPMTF). With the new DMS multi-phase chemistry mechanism, the aerosol dynamics
132 model could capture the observed particle number concentrations and secondary PM MSA
133 and SO_4^{2-} during DMS oxidation experiments performed at both dry and humid conditions at
134 0 ºC and 20 ºC in the AURA chamber. For more details on the DMS, halogen and multi-phase
135 chemistry scheme used in ADCHEM, the reader is referred to the article and supplement of
136 Wollesen de Jonge et al., (2021).

137 The aim of this work is to understand the processes and DMS oxidation products governing
138 the formation and growth of the secondary aerosol in pristine remote marine Arctic region. To
139 facilitate this, we have implemented the above mentioned DMS multi-phase chemistry
140 mechanism into ADCHEM (see Methods section) and modeled the aerosol formation along

air mass trajectories arriving at Ny-Ålesund. We compared the model results with observations from Zeppelin (78°56' N, 11°53' E, 474 m a.s.l) and Gruvebadet (78°92' N, 11°90' E, 67 m a.s.l). These two sites represent remote marine Arctic conditions. Gruvebadet represents ground-level concentrations as it is well within the boundary layer (BL). Zeppelin on the other hand, is most often above the BL in winter months and sometimes below the BL during spring and summer months (Traversi et al., 2020). This implies that Zeppelin is more influenced by long range transport, and Gruvebadet by more local effects (Traversi et al., 2020). This, demonstrates the complexity involved in capturing the atmospheric mixing and secondary aerosol concentrations at Ny-Ålesund. The reason is that Svalbard has an orographically complex terrain comprising of mountains, glaciers, fjords and flat lands that introduce various micro-meteorological phenomena (Rader et al., 2021; Schemann and Ebell, 2020).

2. Methods

Using the combined multi-phase DMS chemistry mechanism by Wollesen de Jonge et al., (2021), MCMv3.3.1 and the monoterpene peroxy radical autoxidation mechanism (PRAM, Roldin et al., 2019; Xavier et al., 2019) we simulated aerosol particle formation within the marine boundary layer (MBL) upwind and at Ny-Ålesund between 1st - 25h May 2018, using the Aerosol Dynamics, gas and particle-phase CHEMistry and radiative transfer model ADCHEM (Öström et al., 2017; Roldin et al., 2011, 2019). We ran ADCHEM as a Lagrangian model along the air mass trajectories arriving at Zeppelin every 3 hours during the selected period (in total 200 trajectory simulations). FLEXPART v10.4 was used to calculate the air mass trajectories and potential emission sensitivity fields (Pisso et al., 2019; Stohl et al., 2005). The simulation results for the vertical distribution of newly formed aerosol (particle diameters < 12 nm) were validated against concurrent measurement data available from the ALADINA (Application of Light-Weight Aircraft for Detecting in situ Aerosol) campaign, wherein a UAS was used to investigate horizontal and vertical distribution of aerosol profiles in the marine boundary layer (ABL) (Lampert et al., 2020). Additionally, modeled particle number size distributions and PM_{10} chemical compositions were compared to the available measured particle number size distributions and PM_{10} filter samples at both Gruvebadet and Zeppelin measurement stations.

2.1 Air mass trajectories and potential emission sensitivity fields

173 We employed the Lagrangian particle dispersion model FLEXible PARTicle
174 (FLEXPARTv10.4) to assess the emission sensitivities or "footprints" of air-masses origin
175 arriving at Zeppelin during the simulation period. FLEXPART is a stochastic model used to
176 compute dispersion of hypothetical particles, based on mean, turbulent and diffusive flows
177 which can be run backwards in time to estimate air mass history at a site (Pisso et al., 2019).
178 European Center for Medium-Range Weather Forecasts (ECMWF) ERA5 reanalysis
179 meteorology with 137 height levels, 1-hour temporal and 0.5^o x 0.5^o spatial resolution, was
180 used as an input to FLEXPART (*ERA5 hourly data on single levels from 1979 to present.*
181 *Copernicus Climate Change Service (C3S) Climate Data Store (CDS). last access 30th April*
182 *2021, 10.24381/cds.adbb2d47, ERA5 hourly data on pressure levels from 1979 to present.*
183 *Copernicus Climate Change Service (C3S) Climate Data Store (CDS). last access 30th April*
184 *2021, 10.24381/cds.bd0915c6*). The air-mass history was simulated 7-day backwards in time
185 and arriving at Zeppelin (474 m a.s.l) every 3 hours (at 00:00, 03:00, 06:00, 09:00, 12:00,
186 15:00, 15:00 and 21:00 UTC) for the entire simulation period (1st - 25th May 2018).

187 FLEXPART calculated normalized emission sensitivity fields were combined with oceanic
188 emissions (DMS, dibromomethane, tribromomethane, iodomethane), NH_3 from sea-bird
189 colonies and anthropogenic emissions (NH_3, SO_2, CO, NO_x) derived from global inventories
190 (see section 2.2). This was done to obtain representative emissions that consider the complete
191 emsission source regions along the trajectories, upwind of the measurement station.
192 Additional meteorological parameters such as temperature, pressure, sea surface temperature,
193 specific humidity and cloud liquid water content from ERA5 reanalysis dataset were extracted
194 along the trajectories and provided as inputs to ADCHEM.

195

196 **2.2 Gas and primary particle emissions**

197 Emissions of gas-phase biogenic volatile organic compounds (VOCs) α-pinene, β-pinene Δ3-
198 carene, limonene, isoprene and β-caryophyllene were modeled with a 1 - dimensional version
199 of MEGAN v2.04 (Model of Emissions of Gases and Aerosols from Nature 2.04) (Guenther
200 et al., 2006). Gas-phase emissions of marine halogens such as tribromomethane ($CHBr_3$),
201 dibromomethane (CH_2Br_2), iodomethane (CH_3I) were retrieved from CAMS-OCE Global
202 oceanic emissions (CAMS-GLOB-OCE) which are available as daily means with a spatial
203 resolution of 0.5^ox0.5^o (Granier et al., 2019; Ziska et al., 2013). CAMS-GLOB-OCE also
204 provides gas-phase DMS emissions with the same temporal and spatial resolution (Granier et
205 al., 2019) calculated with the air-sea flux parameterization and emission fluxes described in

206 (Lana et al., 2011; Nightingale et al., 2000). NH$_3$ emissions from seabird colonies were

207 acquired from a global emission inventory (Riddick et al., 2012). To account for additional

208 NH$_3$ fluxes from the open ocean, we used an estimated sea surface equilibrium NH$_{3(g)}$

209 saturation concentration of 0.5 nmol/m^3 (12.2 ppt at standard temperature and pressure (STP))

210 which approximately correspond to a surface ocean ammonium concentration of 0.125

211 mmol/m^3 (or ~3ppb, calculated based on equation 3 & 4 from Wentworth et al., 2016) at a sea

212 surface temperature of +2 ºC. The sea surface temperature for the study period varied between

213 -2 ºC-23ºC along the trajectories. The estimated surface ocean ammonium concentrations is in

214 close agreement with the concentration estimated by the global ocean biogeochemical model

215 COBALT (Stock et al., 2014) in the North Atlantic ocean, but up to a factor of ~5 higher than

216 the concentrations simulated with other ocean biogeochemical models and/or model setups

217 (Paulot et al., 2015). Therefore, we performed model sensitivity runs with a sea surface

218 equilibrium NH$_{3(g)}$ concentration of 0.1 and 1 nmol/m^3. The NH$_{3(g)}$ equilibrium saturation

219 concentrations represent the ambient surface gas-phase concentration at which the air-sea flux

220 changes direction, with a net downward flux from air to sea if the ambient NH$_{3(g)}$ exceeds the

221 equilibrium gas concentrations and vice versa (Wentworth et al., 2016). For the anthropogenic

222 trace gas and primary particle emissions, we used the CAMS-GLOB-ANT v2.1 inventory,

223 with a spatial resolution of 0.1°x0.1º (Granier et al., 2019).

224 In this work, we used the sea surface temperature (SST) and wind speed dependent sea-spray

225 aerosol (SSA) emission parameterization by Sofiev et al. (2011), (further referred to as

226 Sofiev11). Sofiev11 used a modified source function based on the parameterization of

227 Monahan et al. (1986) and experiments by Mårtensson et al. (2003) and SEAS campaign by

228 Clarke et al. (2006). The modified source function in Sofiev11 provides extrapolated SSA

229 emissions between size ranges of 10 nm-10 μm, with appropriate correction functions

230 employed for SST deviating from 298.15 K (Sofiev et al., 2011). Sofiev11 SSA

231 parameterization shows that with increasing temperatures, emission flux for larger particles

232 increases while the emission fluxes for smaller particles decreases (Barthel et al., 2019;

233 Sofiev et al., 2011). We performed sensitivity tests using the temperature and wind speed

234 dependent SSA parameterization by Salter et al., (2015), (further referred to as Salter15).

235 Both the Salter15 and Sofiev11 are valid between 10 nm-10 μm. Model simulation

236 comparisons between Sofiev11 and Salter15 have shown that the SSA parameterization from

237 Sofiev11 has a stronger temperature dependence and higher particle number concentration

238 emissions in the Aitken mode but result in lower PM$_{10}$ emissions at temperatures below 25 ºC

239 (Barthel et al., 2019).

240

2.2 ADCHEM

For this study, ADCHEM was employed as a 1 - dimensional column model with 40 logarithmically vertical layers, extending up to ~2600m. The model time step used for simulations was 30 seconds. The vertical atmospheric turbulent diffusion was solved using a modified Grisogono turbulent diffusivity scheme (Jeričević et al., 2010; Öström et al., 2017; Roldin et al., 2019). The ADCHEM aerosol module includes new particle formation, Brownian coagulation, condensation and evaporation of particles, and finally the dry and wet deposition of both particles and gases. The particle number size distributions were represented using 100 size bins ranging from 1.07 nm to 10 μm dry diameter. Clouds were assumed to be present in the model grid cells when the bulk liquid water content (LWC, extracted along the trajectory from ERA5 datasets) was greater than 0.01 g m^{-3}. As a default, we used a constant cloud supersaturation (*S)* of 0.25% and the particles were activated into cloud droplets, if the calculated water vapor supersaturation above the particle surface (S_c, calculated using Köhler theory) was smaller than *S*. For sulfate dominated aerosol particles this corresponds to a minimum dry particle activation diameter of ~80 nm (see Figure S10). During the cloud processing, each activated cloud droplet was assumed to take up an equal amount of liquid water corresponding to the total bulk LWC divided by the calculated number concentration of activated cloud droplets. The gas-liquid droplet mass transfer and dissolution of 50 species in total, including HCl, HNO$_3$, H$_2$SO$_4$, NH$_3$, HIO$_3$, H$_2$O$_2$, O$_3$, OH, BrO, NO$_3$, DMSO, MSIA, MSA and HPMTF and their irreversible reactions in the interstitial and activated cloud droplets are treated by the multi-phase chemistry mechanism (see Wollesen de Jonge et al. (2021) for details). The kinetic pre-processor (KPP) (Damian et al., 2002) was used to generate the multi-phase chemistry mechanism used in this study.

Recent observations of NPF at Ny-Ålesund have confirmed the importance of ion-mediated H$_2$SO$_4$-NH$_3$ nucleation in spring with MSA and H$_2$SO$_4$ condensation contributing to the subsequent growth of particles (Beck et al., 2021; Lee et al., 2020). In this work, the Atmosphere Cluster Dynamics Code (ACDC) (McGrath et al., 2012; Olenius et al., 2013) was coupled with ADCHEM (Roldin et al., 2019). ACDC was used to model NPF, which involved H$_2$SO$_4$ clustering with NH$_3$ via both neutral and ion-induced pathways with an ionization rate of 1.7 cm^{-3}s^{-1}. ACDC was used to solve the evolution of molecular H$_2$SO$_4$-NH$_3$ clusters by considering the loss of clusters by collisions, evaporation or coagulation scavenging onto larger aerosol particles. At each time step, the flux of clusters (up to ~ 5

273   H_2SO_4 and 5 NH_3 each) growing out of the ACDC molecule-cluster domain represents the

274   NPF rate. These newly formed clusters are assigned to the corresponding smallest particle

275   size bin at 1.07 nm in diameter in ADCHEM, which then simulates the condensational growth

276   of particles and losses due to evaporation, coagulation, and wet and dry deposition.

277   For all simulations, we used model output from the closest height levels which can represent

278   Gruvebadet (model height of 73.5 m a.s.l) and Zeppelin (model height of 486.0 m a.s.l).

279   **Sensitivity Tests**

280   Alongside the main ADCHEM simulations, *BaseCase,* we performed nine complementary

281   scenario runs to assess the impact of different processes on the modeled aerosol

282   concentrations. We performed simulations without aerosol in-cloud processing (*Cloudoff*), to

283   check the impact of in-cloud processing on the growth of aerosols. We investigated the effect

284   of higher PM_{10} particle emissions on the chemical composition of secondary aerosols, using

285   the sea-spray emission parameterization based on Salter et al., 2015 (*SalterSSA*). Simulations

286   were conducted to assess the impact of lower and higher ammonia sources over the open

287   ocean (*LowNH₃, HighNH₃*). A sensitivity test without precipitation (*NoPrecip*) was performed

288   to test the influence of precipitation on number concentration and particle composition. Since

289   cloud supersaturation is critical to the activation of particles and is highly uncertain, we

290   performed two simulations with low and high cloud supersaturation (*S=0.1%*, *SSat=0.1* and

291   *S=0.4%*, *Ssat=0.4*) to test its impact on the modelled particle distributions. This corresponds

292   to minimum dry particle activation diameters of ~150 nm and ~60 nm respectively, for sulfate

293   rich aerosol particles (see Figure S10). We performed a simulation without new particle

294   formation (*NPFoff*), and finally one simulation without the dissolution and irreversible

295   aqueous chemistry of the intermediate DMS oxidation products, SO_2 and halogens

296   (*woDissolution*), implying that MSA, H_2SO_4 and HIO_3 is only formed in the gas-phase. Table

297   1. summarizes the setup for different model sensitivity test.

298

299   **Table 1.** Model sensitivity tests performed alongside the main *BaseCase* simulations to test

300   the effect of different parameters on secondary aerosol formation. These sensitivity tests focus

301   on the role of in-cloud processing and aqueous phase chemistry, the NH_3 emissions from open

302   ocean, SSA parameterization and cloud supersaturation. The sea surface equilibrium $NH_{3(g)}$

303   concentrations in ppt are provided in the brackets.

Simulation	In-cloud	$NH_{3(eq)}$ (nmol/m³,	SSA	Precipitation

	Processing	ppt)	parameterization	
BaseCase	On	0.5 (12.2)	Sofiev11	On
SalterSSA	On	0.5 (12.2)	Salter15	On
Cloudoff	On	0.5 (12.2)	Sofiev11	On
LowNH₃, HighNH₃	On	0.1 (2.4) 1.0 (24)	Sofiev11	On
NoPrecip	On	0.5 (12.2)	Sofiev11	Off
SSat0.4, SSat0.1	On	0.5 (12.2)	Sofiev11	On
NPFoff	On	0.5 (12.2)	Sofiev11	On
WoDissolution	On, but no dissolution and irreversible chemistry of intermediate DMS oxidation products	0.5 (12.2)	Sofiev11	On

304

2.3 Measurements

305

306 We utilized comprehensive measurements from the Ny-Ålesund Research station sites,
307 Zeppelin observatory (Platt et al., 2022) and Gruvebadet during the period of 1st - 25th May
308 2018. Since 2017, the atmospheric observatory at Gruvebadet, which is located about 700 m
309 southwest of Ny-Ålesund village at almost sea level (67 m.s.l), hosted Neutral cluster and Air
310 Ion Spectrometer (NAIS, Manninen et al., 2010; Mirme and Mirme, 2013) for semi-
311 permanent measurements. Here we use NAIS measured number size distribution of naturally
312 charged (ions) in diameter size ranges between 0.8 nm-40 nm and neutral particles in the size
313 range of 2.5 nm-42 nm, with a temporal resolution of two seconds.

314 During the measurement period, a scanning mobility particle sizer (SMPS), was operated to
315 measure particle number size distribution in the diameter size range of 10 - 470 nm at
316 Zeppelin. Concurrent SMPS data (TSI 3034, 54 channels) with diameter size ranging from 10
317 to 470 nm from Gruvebadet were also available (Dall'osto et al., 2019b; Moroni et al., 2020),
318 thus, enabling us to compare the modeled particle number size distribution with the measured
319 size distributions at both measurement stations. Daily resolution continuous aerosol samples
320 with PM_{10} cutoff were collected at Gruvebadet using a Tecore Skypost low-volume sampler
321 (Amore et al., 2022). The detection limit for Na^+ was 0.0001 μg m^{-3} and 0.0002 μg m^{-3} for Cl^-,

322 NH_4^+ and SO_4^{2-}. Since the field blank medians at Gruvebadet were less than 1 percentile of

323 sampled values, the field blanks were not subtracted from the sampled values (Amore et al.,

324 2022).

325 Vertical particle number concentration profiles were obtained using UAS ALADINA (Bärfuss

326 et al., 2018; Lampert et al., 2020), which was operated during the simulation period.

327 ALADINA were operated up to a height of 850 m a.s.l., thus can be used for a potential

328 closure between the two different research sites of Gruvebadet and Zeppelin. ALADINA is

329 equipped with two condensation particle counters (CPCs Model 3007, TSI Inc., St. Paul,

330 MN, USA), measuring in the size ranges of 3 nm - 2 μm (CPC1) and ~12 nm - 2 μm (CPC2)

331 (Lampert et al., 2020; Petäjä et al., 2020) . The difference between CPC1 and CPC2 provides

332 an estimate of particle number concentrations in the size of 3 - 12 nm (N_{3-12}), which was used

333 as an indicator of NPF. Alongside the CPCs, a host of other instruments measuring

334 meteorological parameters were operated in unison, the description of which can be found in

335 Bärfuss et al., (2018) and Lampert et al.,(2020).

336 **Evaluating temporal aspects of model performance**

337 The modeled PM_{10} inorganic chemical composition was evaluated against the measured PM_{10}

338 inorganic chemical composition using statistical estimates such as, normalized mean bias

339 (NMB), Pearson correlation coefficient (r), root mean squared error (RMSE) and fraction of

340 predictions within a factor of 2 of the observed values (FAC2). These tests were used to

341 evaluate modeled values (M_i) against observation values (O_i) at both the measurement sites.

342 Pearson correlation coefficient was calculated using the formula:

343
$$r = \frac{1}{n} \sum_{i=1}^{n} \frac{\left(O_i - \bar{O}\right)}{\sigma_O} \frac{\left(M_i - \bar{M}\right)}{\sigma_M} \qquad \text{(Eq 1)}$$

344

345 Where σ_O and σ_M are standard deviations of the observed and modeled values, respectively.

346 Normalized mean bias (NMB) indicates if the predictions are over or underestimating the

347 observed values, with the factor representing the under or over estimation. NMB was

348 calculated using Eq. 2:

349
$$NMB = \frac{\sum_{i=1}^{n}(M_i - O_i)}{\sum_{i=1}^{n} O_i} \qquad \text{(Eq 2)}$$

350

351 Root mean squared error (RMSE) was calculated using Eq. 3:

$$RMSE = \sqrt{\sum_{i=1}^{n} \frac{(M_i - O_i)^2}{n}}$$ (Eq 3)

352

353

354 FAC2 is a robust metric defined as the percentage of predictions which are within a factor of

355 2 of the observed values (Eq. 4):

356   (Eq 4)

$$Fac2 = 0.5 \leq \frac{M}{O} \leq 2.0$$

357 **3. Results and Discussion**

358 In the following sections, we analyze and evaluate the model results against comprehensive

359 measurements in Ny-Ålesund. In sub-section 3.1, we focus on the particle number size

360 distributions at both sites, followed by gas-phase concentrations and PM_{10} inorganic chemical

361 composition (sub-section 3.2) and the vertical nano-particle concentration profiles (sub-

362 section 3.3). Finally, in sub-section 3.4, we analyze the results from the model sensitivity

363 tests.

364

365 **3.1 Particle number size distributions**

366 Figure 1(a) and (b) show the observed and predicted particle number size distributions at

367 Gruvebadet for the *BaseCase* simulation. Figure 1(a) includes SMPS observations starting

368 from 10 to 470 nm and NAIS observations for neutral particles in the range 2.5 nm-10 nm

369 (boundary marked by the black line) since NAIS data below 2.5 nm cannot be relied upon,

370 owing to the presence of corona generated ions (Jayaratne et al., 2017; Manninen et al., 2011,

371 2016).

372 In the *BaseCase* simulationsthe model captures particle formation on 2nd May followed by an

373 increasing number of Aitken and accumulation mode particles during the days of 3rd - 4th

374 May, which is the result of more polluted air masses arriving at Ny-Ålesund from the

375 European continent (Figure S1). Similarly, the model reproduces the particle formation on the

376 20th of May, specifically in the size ranges 2-8 nm, but overestimates the Aitken mode and

377 accumulation mode particle concentration on the 21st of May. However, the model tends to

378 underestimate the nucleation mode particle number concentrations between 10-25 nm (N_{10-25}

379 $_{nm}$) around noon, and overestimate the concentrations during the morning and evening (Figure

380 S2a). The model and measurements show an apparent time delay in the formation of new

381 particles larger than 10 nm. While the measurements show a peak at 11 am the simulated $N_{10\text{-}25\,nm}$

382 shows a maximum at 3 am and 6 pm. The modeled $N_{10\text{-}25\,nm}$ maximum around 6 pm is

383 likely a result of the formation of new particles around noon, which grow to >10 nm in

384 diameter during the afternoon and evening by condensation of H_2SO_4. The predicted Aitken

385 ($N_{25\text{-}100\,nm}$) and accumulation mode particle concentrations ($N_{>100\,nm}$) which form few days

386 upwind of the station are overall, in good agreement with the measurements, which show a

387 minor diurnal trend (Figure 2b-c). The measurements indicate that at Gruvebadet, $N_{10\text{-}25\,nm}$

388 contributes the most significant fraction of measured total number concentrations with 45.3%,

389 while $N_{25\text{-}100\,nm}$ and $N_{100\text{-}470\,nm}$ contribute 30.5% and 23.94% respectively. However, the

390 simulations predict greater contribution of Aitken mode (~53.85%) to total number

391 concentration, with the $N_{10\text{-}25\,nm}$ and $N_{100\text{-}470\,nm}$ accounting for ~ 36.58% and 9.57%

392 respectively (Figure S2).

393 Figure 2 shows the measured size distribution in panel (a) and simulated size distribution in

394 panel (b) for Zeppelin. At Zeppelin, the model overestimates the number concentration in

395 nucleation and Aitken modes (also cf. Figure S3, supplementary). The particle number size

396 distribution measurements at Zeppelin indicate that the relative contribution of the three

397 modes (nucleation, Aitken and accumulation) varies to some extent when compared to

398 Gruvebadet. Measurements show that at Zeppelin, $N_{10\text{-}25\,nm}$ contributes ~33.46%, $N_{25\text{-}100\,nm}$

399 46.43% and $N_{>100\,nm}$ 20.11% to the total particle number concentrations. The model predicts

400 lower relative contribution of $N_{10\text{-}25\,nm}$ (26.94%), and a greater contribution of $N_{25\text{-}100\,nm}$

401 (63.44%) to the total simulated particle number concentrations. The diurnal trends at Zeppelin

402 agree well with earlier measurements conducted at Zeppelin in spring by Ström et al. (2009).

403 Additionally, the measured diurnal pattern at Zeppelin varies in comparison to Gruvebadet. At

404 Zeppelin, the $N_{10\text{-}25\,nm}$ concentrations peak in the afternoon and evening. The modeled

405 $N_{10\text{-}25\,nm}$ shows only a weak diurnal trend. It should be noted that the measurements show a

406 time delay of around 3 hours in the peak $N_{10\text{-}25\,nm}$ concentrations at the two sites (Figure S2

407 and S3). This is possibly be a result of vertical mixing and dilution effects modulating the

408 observed particle number concentrations at sites situated at different altitudes, similar to

409 observation made at Zeppelin and Corbel by Ström et al. (2009).

410 ADCHEM considers the formation of new particles via both the ion-mediated and neutral

411 H_2SO_4 -NH_3 clustering pathways. Beck et al (2021) observed dominant contribution of

412 negatively charged H_2SO_4 -NH_3 clusters to secondary particle formation in May 2017 at Ny-

Ålesund, with HIO$_3$ playing a small role in the initial particle formation. However, the discrepancy in the modeled and observed diurnal trends of $N_{10\text{ - }25\text{ nm}}$ could indicate that there are other sources or vapors that might potentially contribute to the particle formation. Other possible NPF mechanism may involve amines (Olenius et al., 2013) and pure biogenic highly oxidized molecule (HOM) (neutral and ion induced) nucleation (Kirkby et al., 2016). We speculate that the exclusion of these other mechanisms (HIO$_3$, H$_2$SO$_4$-amines and HOM driven particle formation) might result in the discrepancies in the modeled and observed particle number concentration diurnal trends. HIO$_3$ induced particle formation could, e.g. play an important role if the air masses upwind of Ny-Ålesund traverse over the sea-ice covered regions (Baccarini et al., 2020; Beck et al., 2021).
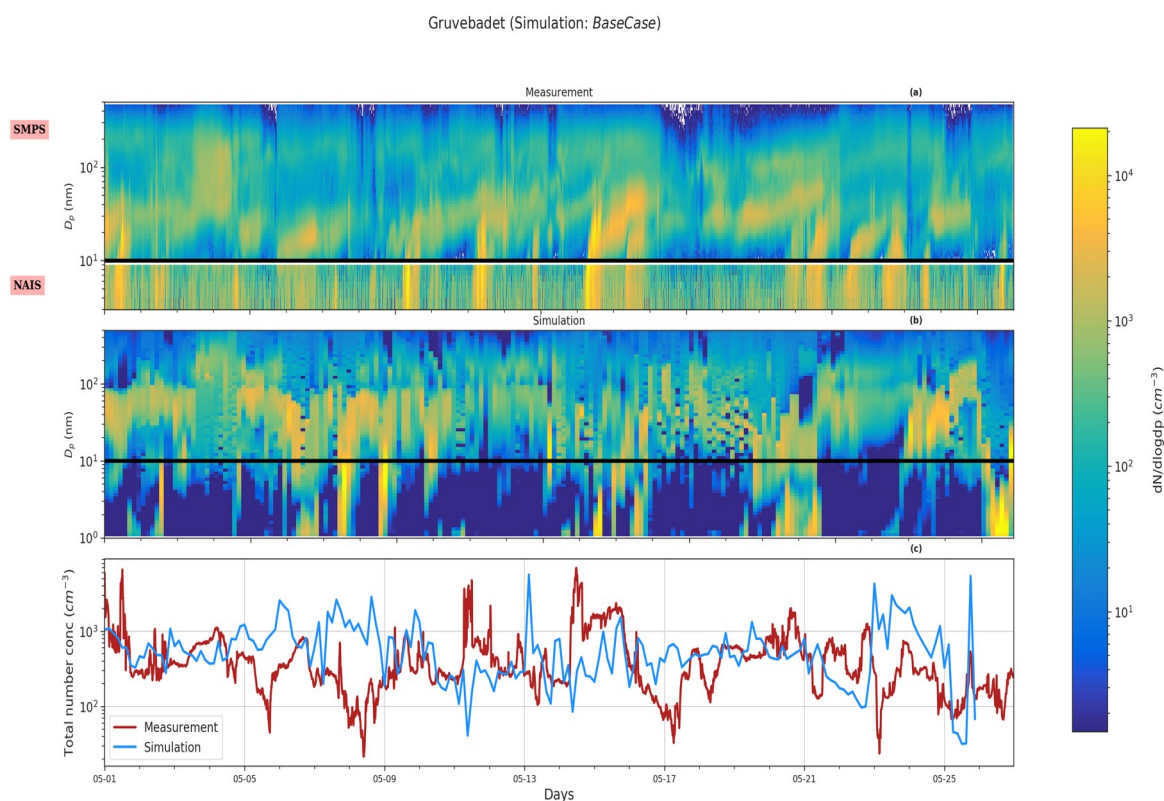
Figure 1. Particle number size distribution at Gruvebadet for *BaseCase*. The panel **(a)** shows the measurement data for the period 1-25th May from SMPS (10 nm-470 nm) and NAIS (2.5 - 10 nm), the panel **(b)** provides the modeled particle size distribution and panel **(c)** shows the total measured and simulated number concentrations. The black line at 10 nm denotes the boundary above which SMPS data starts and NAIS data ends. The abscissa indicates the time for the entire simulated duration. The ordinate in Figure 1 for both panels (a) and (b) indicates the particle diameter (D$_p$, nm).
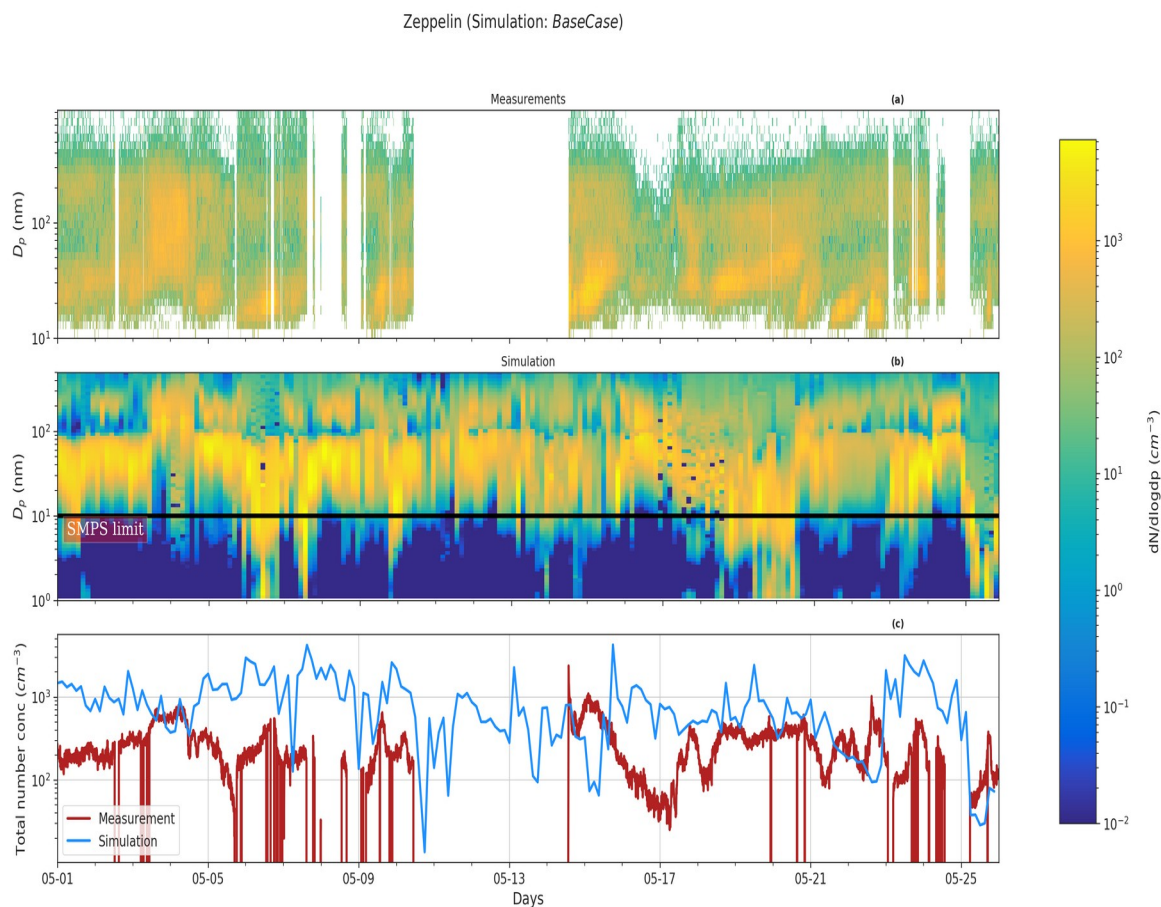
Figure 2. Particle size distribution at Zeppelin. The panel **(a)** shows the measurement data for the period 1-25th May from SMPS, the panel **(b)** provides the simulated particle size distribution and panel **(c)** shows the total measured and simulated number concentrations for the *BaseCase* simulations. The abscissa and ordinates are similar to Figure 1.

Figure 3 presents the median particle number size distribution for the *BaseCase* simulation at both Zeppelin and Gruvebadet, with respective 25th and 75th percentiles, for the entire selected period. At Gruvebadet, the modeled and measured median particle number size distributions are in reasonable agreement for both Aitken and accumulation mode. However, the model over predicts the median Aitken mode concentrations at Zeppelin by a factor ~ 5.5. The modeled Aitken mode peak at both measurement sites is ~50 nm, while the measured Aitken mode peak is ~30 nm. Though the modeled accumulation mode peak is at a larger size (~150 nm), compared to the measured accumulation mode peak (~110 nm), the predicted value is slightly lower than the monthly averaged accumulation mode peak location measured at Zeppelin in earlier studies (~160-170 nm, Dall'Osto et al., 2019).

The discrepancy between the modeled and measured particle concentrations at Zeppelin can be caused by the underlying complexity of modeling the boundary layer dynamics at an elevated site, such as Zeppelin. The vertical mixing of aerosols along the up-slope or down-slope of a mountain site is difficult, if not impossible for a 1- dimensional column model, since it is unable to capture the topographical influence on locally varying wind speeds or latent and sensible heat fluxes (Mikkola, 2020; Wainwright et al., 2012).
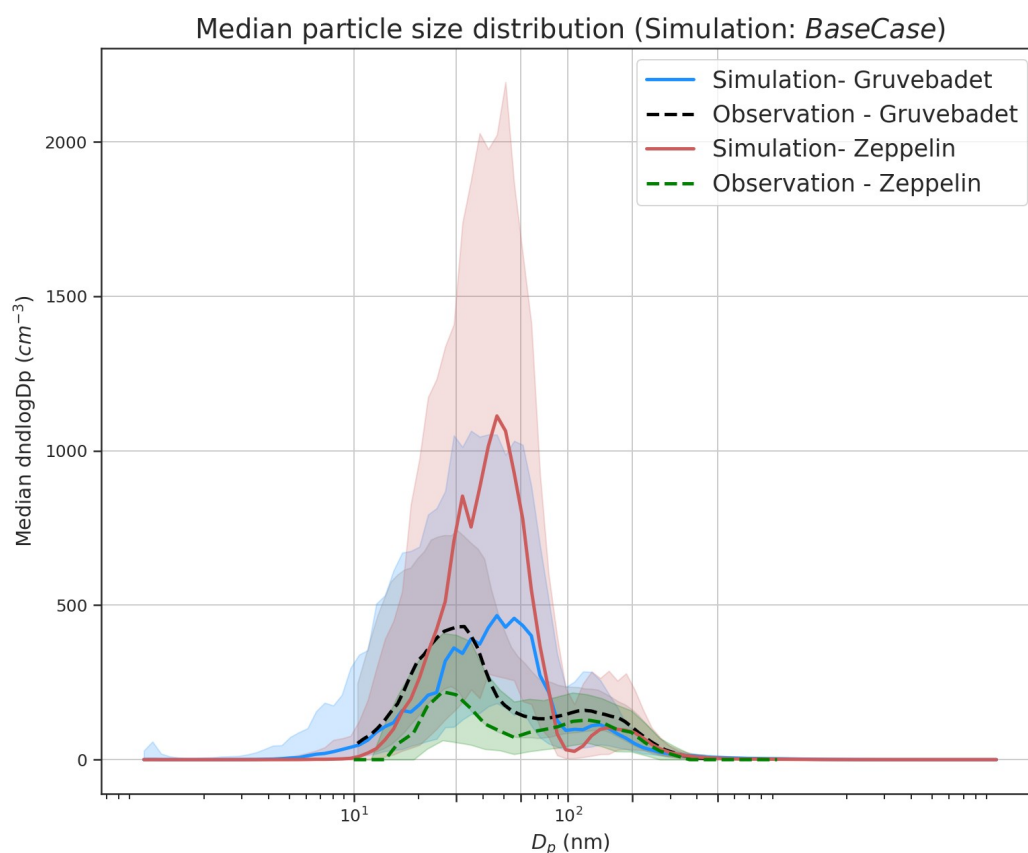
Figure 3. Median particle number size distribution at Gruvebadet and Zeppelin for both modeled (*BaseCase* simulations) and measured values. The shaded areas indicate the 25th and 75th percentiles for both model and measured median particle number size distribution. At Zeppelin, the simulated median size distribution is calculated for periods only when SMPS data were available.

Another detectable feature in the median particle number size distribution is the diameter of the Hoppel minimum (Hoppel et al., 1985, 1986), and the role of in-cloud processing in forming this minimum. A Hoppel minimum is often observed in marine air masses (Fossum

461 et al., 2018; Tunved et al., 2013; Zheng et al., 2018) and is attributed to in-cloud processing of

462 aerosols, with chemical processing (e.g., sulfate production via oxidation of dissolved SO_2)

463 (Feingold and Kreidenweis, 2000; Hoppel et al., 1986), and coalescence of droplets playing a

464 key role (Flossmann and Wobrock, 2019; Hoppel et al., 1986; Hoppel and Frick, 1990; Noble

465 and Hudson, 2013). It has been estimated that, on average, aerosols take part in about 10 non-

466 precipitating cloud cycles before it is removed from the atmosphere by wet scavenging

467 (Hoose et al., 2008; Hoppel et al., 1986; Rosenfeld et al., 2014). These non-precipitating

468 cloud cycles facilitate the formation of hygroscopic accumulation mode particles, with low

469 critical supersaturation (S_c) that readily activates to cloud droplets during subsequent cloud

470 cycles, thus growing to larger sizes. This is because the activated particles undergo chemical

471 processing, gas-to-particle conversions, coalescence and coagulation with other interstitial

472 particles. Upon evaporation of water, the emerging dry particles have a larger size and lower

473 S_c, leading to a minimum being formed between the un-activated and activated cloud droplets

474 (Herenz et al., 2018; Hudson et al., 2015; Noble and Hudson, 2013). The diameter at which

475 the Hoppel minimum is observed varies depending on the cloud supersaturation and particle

476 composition (Hoppel et al., 1986; Hudson et al., 2015), with Hoppel minima sizes observed in

477 ranges from 60 nm at Zeppelin Ny-Ålesund to around 90 nm at Tuktoyatuk, Canada (Herenz

478 et al., 2018; Tunved et al., 2013).

479 The median particle number size distribution in Figure 3 shows that at both stations, the

480 measured Hoppel minima is around ~ 60 nm, while the simulated Hoppel minima are around

481 the size of ~ 100 nm at both sites. This difference in location of Hoppel minima can be

482 attributed to the assumed value of S=0.25% in the model. The value of S used in the model

483 lies in the range of typical marine stratocumulus clouds, which can vary between 0.1 - 1%

484 (Fossum et al., 2018; Quinn et al., 2017). With S=0.25% the sulfate dominating particles in

485 the Arctic marine boundary layer will be activated into cloud droplets if their diameter is

486 greater than ~85 nm in diameter (Fig. S10).

487 **3.2 Gas and particle-phase chemical composition of important precursors**

488 Figure 4 shows the range of simulated gas-phase concentrations of DMS oxidation products

489 H_2SO_4, MSA and HIO_3 for the entire period at height levels representing Gruvebadet. The

490 mean measurement values (red dots) represent gas-phase concentrations for the same species

491 from an earlier 2017 May campaign performed at Gruvebadet by Beck et al., (2021).

492 Measurements of H_2SO_4 at Gruvebadet from May 2017 indicate monthly mean concentrations

493 around ~10^6 # cm^{-3} (Beck et al., 2021). The modeled H_2SO_4 concentrations at Gruvebadet are

494 3×10^6 # cm^{-3}, implying a reasonably good model performance in predicting gaseous

495 precursor concentrations. The simulated gas concentrations of MSA (10^5-10^8 # cm^{-3}) also

496 agrees well with the measurements made at Gruvebadet in May 2017 by (Beck et al., 2021),

497 wherein they measured daily averages of MSA gas concentrations in the order of 10^7 # cm^{-3}.

498 The low modeled values of MSA and DMSO gas phase concentrations at the height

499 representing Zeppelin (c.f. Figure S4 supplementary e.g. between 15/05 - 17/05) coincide

500 with the period where the planetary boundary layer height (PBLH) is below the altitude of

501 Zeppelin station (cf. Figure S5 supplementary). Overall, we can conclude that the modeled

502 precursor gas concentrations at the two measurement sites are, in general, good agreement

503 with earlier measurements at the two sites.
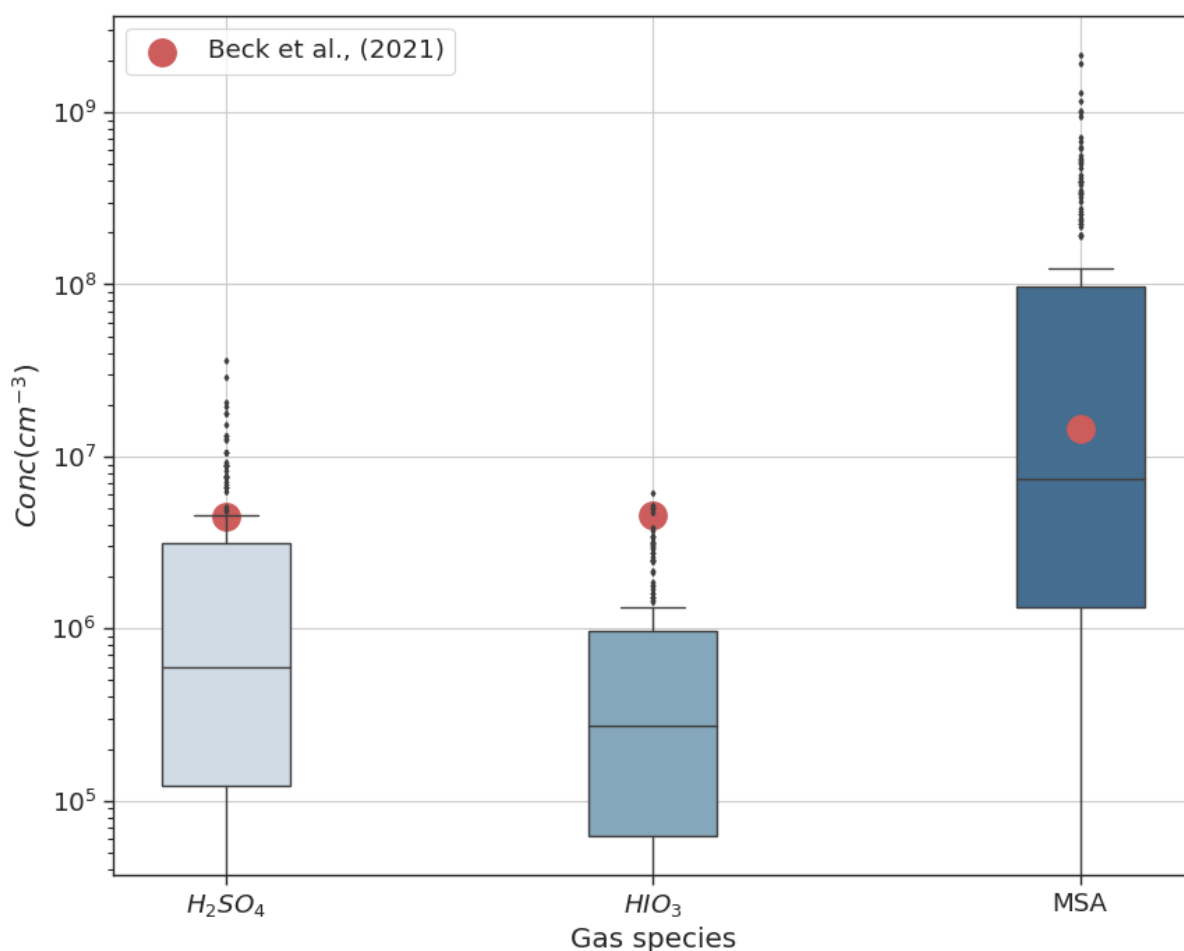
504 **Figure 4.** Gas-phase concentrations at Gruvebadet for the *BaseCase* simulations. The red dots

505 indicate the mean measured values from an earlier 2017 May campaign conducted at

506 Gruvebadet by Beck et al., (2021).

507 Figure 5 (a) shows the simulated median mass size distribution of compounds Cl$^-$, Na$^+$, MSA,

508 SO$_4^{2-}$, NH$_4^+$, and NO$_3^-$ for the *BaseCase* runs in the lowest model layer. Figure 5(a) indicates

509 that the nucleation mode particles are composed mainly of SO$_4^{2-}$ and NH$_4^+$, while MSA, Cl$^-$

510 and Na^+ dominate PM for larger particles. The observed and modeled high $MSA_{(g)}$
511 concentrations in comparison to $H_2SO_{4(g)}$ at Ny-Ålesund is not reflected in the respective
512 vapor contribution to the nano-particle growth. This is because, in contrast to H_2SO_4, MSA is
513 not a non-volatile condensable compound. The gas-to-particle partitioning of MSA requires
514 co-condensation and dissolution of (NH_3) (Hodshire et al., 2019) or the existence of cations
515 such as Na^+ which decreases the particle acidity ($[H^+]$). Figure 5(b) shows the relative mass
516 fraction of the above-mentioned compounds to PM at different sizes. SO_4^{2-} and NH_4^+
517 dominate the mass for particles in the nucleation and Aitken mode. SO_4^{2-} contributes ~74%
518 and ~71% to nucleation and Aitken mode PM, with its contribution decreasing for
519 accumulation (100 nm-1 μm) and coarse (>1 μm) mode PM (~6% and 3.36% respectively)
520 (Table S1). NH_4^+ contribution follows a similar trend, as SO_4^{2-}, with 12.34% and 6.95%
521 contribution to nucleation and Aitken mode PM, but insignificant for accumulation and coarse
522 mode PM (Table S1). The loss of primary sea spray aerosols due to wet scavenging promoted
523 the growth of secondary aerosol particles in the nucleation and Aitken mode by NH_4^+ and
524 SO_4^{2-} as seen in Figure 5 (b). Na^+ (~32.9%), Cl^- (~39.5%) and MSA (20.45%) are the
525 dominant contributors to accumulation and coarse mode PM. In the *BaseCase* simulations,
526 gas-phase SO_2 dissolves in the cloud droplets, and is oxidized by H_2O_2 into SO_4^{2-} (Wollesen
527 de Jonge et al., 2021). Previous modeling studies have shown that a very small fraction of
528 MSA is formed in the gas phase. Instead, most MSA is formed via ozonolysis of MSIA in the
529 aqueous phase (Hoffmann et al., 2016; Wollesen de Jonge et al., 2021). It should be noted that
530 HIO_3 and NO_3^- have an insignificant contribution to total PM_{10}, amounting to ~0.05% and
531 0.17% respectively.

Median mass size distribution and relative mass fraction (Simulation: *BaseCase*)
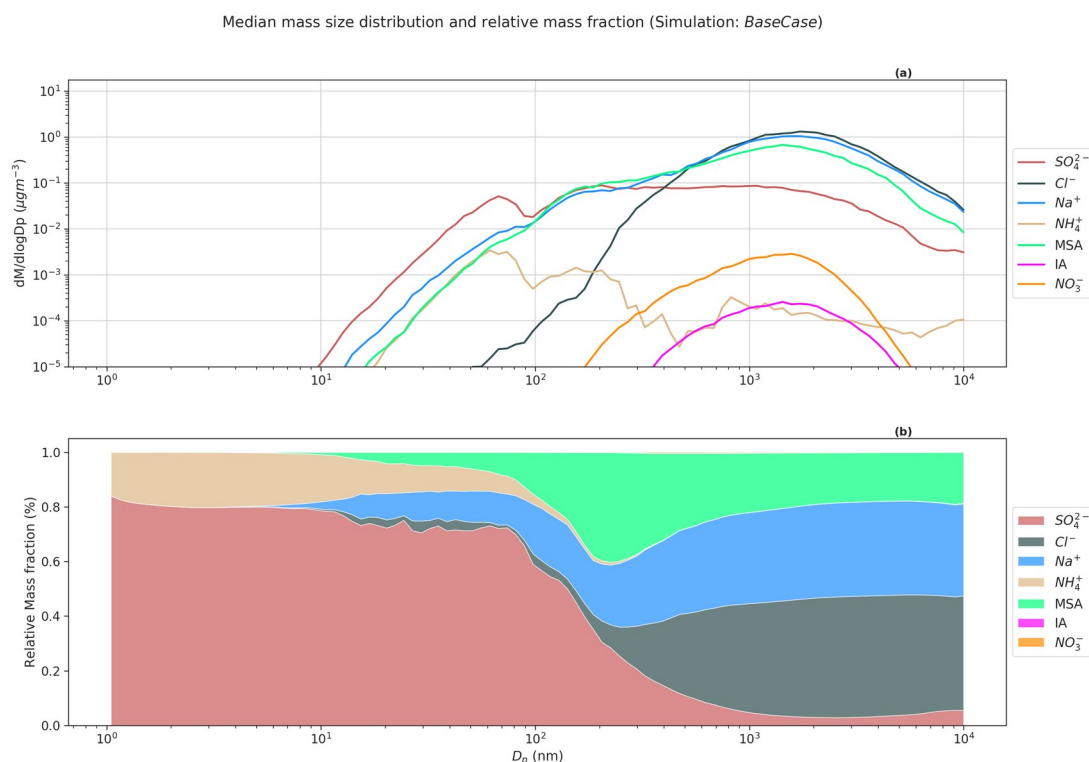
Figure 5. Simulated median mass size distribution for *BaseCase* simulations. The upper panel
(a) shows the median mass size distribution for compounds Cl^-, Na^+, MSA, SO_4^{2-}, NH_4^+, HIO_3
and NO_3^- for the entire size distribution ranging from 1.07 nm-10 μm. The lower panel (b)
shows the relative mass fractions or contribution of compounds Cl^-, Na^+, MSA, SO_4^{2-}, NH_4^+,
HIO_3 and NO_3^- to total non-refractory PM at different sizes.

Figure 6 compares the daily PM_{10} filter measurements to the modeled values at both
measurement stations. The model prediction of PM_{10} Cl^-, Na^+, SO_4^{2-} and NH_4^+, was
evaluated using statistical metrics such as NMB, FAC2, correlation coefficient (*r*) and RMSE
(Table 3). Though the model does well in simulating the trends of PM_{10} SO_4^{2-}, Na^+ and Cl^- at
Zeppelin (*r* values of 0.35, 0.51 and 0.6 respectively), it is unable to predict the NH_4^+ trends
accurately (*r* = -0.08).

Pearson correlation (*r* -values) at Gruvebadet are in the range of 0.29-0.34 for PM_{10} NH_4^+,
SO_4^{2-}, Na^+ and Cl^- implying that the model trends are reasonably consistent with the measured
trends. However, at Gruvebadet the NMB values for PM_{10} NH_4^+ and SO_4^{2-} are underpredicted
(NMB = -0.88 and -0.28 respectively), while PM_{10} Na^+ and Cl^- show a large overprediction
(1.81 and 1.05) in the modelled values. In contrast, at Zeppelin, the modeled PM SO_4^{2-} is
overestimated (NMB=1.96). Likewise, large RMSE and negligible FAC2 values, for PM_{10}
Na^+, and Cl^- imply discrepancies between the predicted and measured values, indicating that
the model is overestimating PM_{10} SO_4^{2-}, Na^+ and Cl^- at Gruvebadet and PM_{10} SO_4^{2-} at

551 Zeppelin. In summary, the model tends to overpredict PM_{10} Na^+, Cl^- and SO_4^{2-} concentrations,

552 but on the other hand, does reasonably well in predicting the daily measured trends.

553 Additionally, the modeled PM_{10} Cl^-/Na^+ molar ratio at Gruvebadet and Zeppelin is ~0.79 and

554 ~0.95, respectively. This is much higher than the observed PM_{10} Cl^-/Na^+ molar ratio at both

555 sites (~0.39). One likely reason for this is the overestimated sea spray aerosol emissions. The

556 PM_{10} Cl^-/Na^+ molar ratios give a measure of the acidic nature of aerosol, since increased

557 condensation of strong acid MSA and H_2SO_4 increases acidity of aerosols thereby causing

558 loss of Cl^- (dechlorination) as HCl (Ayers et al., 1999; Frey et al., 2020). Thus, increased

559 availability of H_2SO_4 and MSA in particle phase in Aitken mode particles results in acid-

560 induced Cl^- loss from sea-spray particles.

561
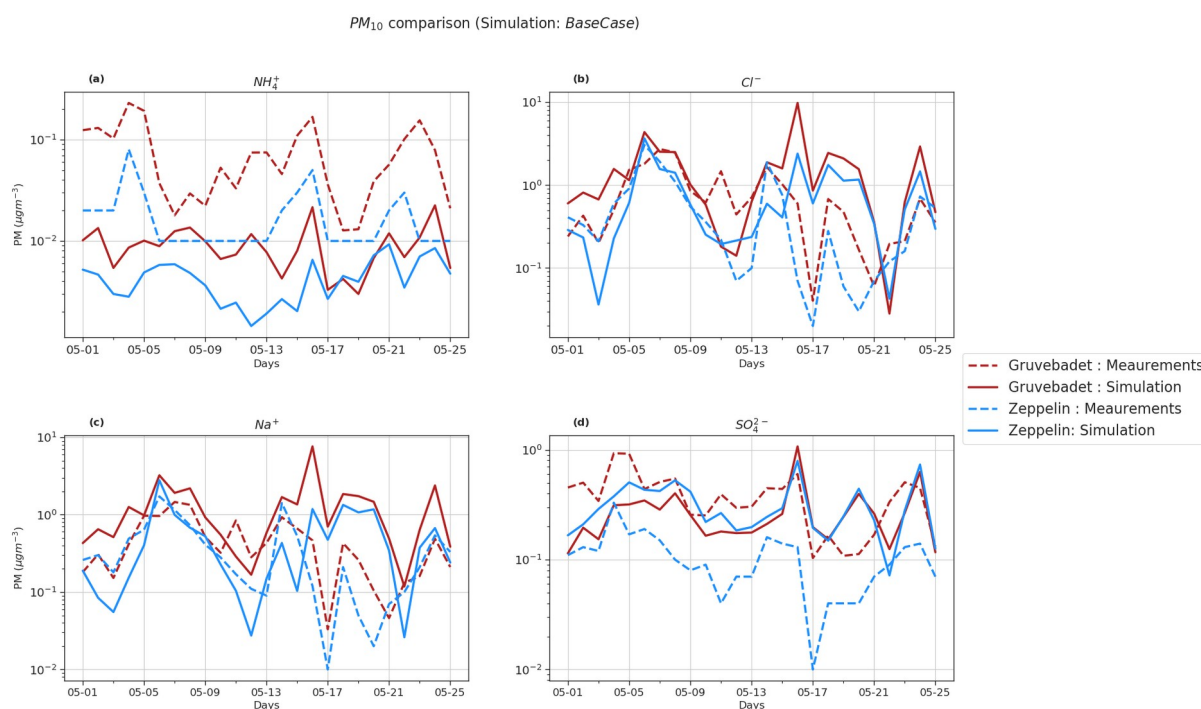
562 **Figure 6.** PM_{10} comparison of *BaseCase* simulations with daily filter samples from

563 Gruvebadet and Zeppelin for the entire modeled period. Panel **(a)** shows PM_{10} NH_4^+, **(b)**

564 shows PM_{10} Cl^-, **(c)** shows PM_{10} Na^+ and **(d)** shows PM_{10} SO_4^{2-} filter samples. The dotted

565 lines in each panel indicate measurement values, and the solid line denotes simulated values.

566 The ordinate is plotted in log scale to better visualize the low values.

567

568 **Table 3**: Evaluation of modeled PM_{10} values at both sites of Gruvebadet (G) and Zeppelin (Z)

569 for the four particle-phase species Cl^-, Na^+, SO_4^{2-} and NH_4^+.

Species	Normalized mean	Correlation	RMSE (µg m⁻³)	FAC2

	bias factor (NMB)	coefficient (r)		
NH_4^+	-0.88^G , -0.76^Z	0.34^G, -0.08^Z	0.09^G, 0.02^Z	0.04^G, 0.2^Z
SO_4^{2-}	-0.28^G, 1.96^Z	0.33^G, 0.35^Z	0.27^G, 0.26^Z	0.6^G, 0.24^Z
Na^+	1.81^G, 0.36^Z	0.29^G, 0.51^Z	1.67^G, 0.55^Z	0.4^G, 0.48^Z
Cl^-	1.05^G, 0.39^Z	0.24^G, 0.60^Z	2.08^G,0.74^Z	0.24^G, 0.44^Z

570

3.3 Vertical profiles of ultra-fine particle

572 Figure 7 (a) shows the measured vertical $N_{3\text{-}12\,nm}$ concentrations from CPC onboard the UAS

573 for four measurement periods overlayed onto simulated vertical profiles. Figure 7 (b) and (c)

574 show the mean vertical profiles for $N_{3\text{-}12\,nm}$ and $N_{>12\,nm}$ for both the *BaseCase* simulation and

575 UAS measurements for the entire selected period. The model underestimates the measured $N_{3\text{-}}$

576 $_{12\,nm}$ and $N_{>12\,nm}$ vertical particle number concentrations below 200 m a.s.l. The NMB for $N_{3\text{-}12}$

577 $_{nm}$ and $N_{>12\,nm}$ is -0.28 and -0.14, respectively, implying that the model underestimates the

578 particle number concentrations. Both the modeled and measured mean particle number

579 concentrations for $N_{3\,\text{-}\,12nm}$ and $N_{>12nm}$ are in good agreement between the heights of 200-600

580 m a.s.l. The lower calculated concentrations of modeled mean particle number concentrations

581 above 600 m a.s.l is most likely affected by higher turbulence in the transition zone from the

582 boundary layer to the free troposphere, which might cause a large mixing of aerosol particles.

583 It should be noted that, at Gruvebadet, the mean SMPS particle number concentrations are in

584 good agreement with the modeled particle number concentrations. However, at the altitude of

585 the Zeppelin station, both the model and UAS measurements of $N_{>12nm}$ are substantially

586 higher (factor of 4) than the mean particle number concentrations measured with the SMPS at

587 Zeppelin. This finding further strengthens the conclusion that the complex orography at Ny-

588 Ålesund highly affects the variability in the vertical scale, which may cause this discrepancy

589 in the observed and modeled particle number concentrations at Zeppelin (see section 3.1). The

590 UAS measurements were carried out at the airport on Ny-Ålesund (and the UAS was flown

591 around Ny-Ålesund) where the boundary layer measurements, like the model, most likely

592 resemble the general Arctic marine boundary layer conditions. Figure S9 shows the influence

593 of different sensitivity simulations on the modeled vertical particle number concentrations.

594 The large spread in the modeled vertical particle number concentrations in Figure S9,

595 highlights the importance of constraining uncertain parameters such as cloud supersaturation

596 and NH_3 gas emissions, to better simulate secondary aerosol formation in marine polar

597 regions.

Vertical profiles for measured and modeled N_{3-12nm} (runtype: BaseCase)
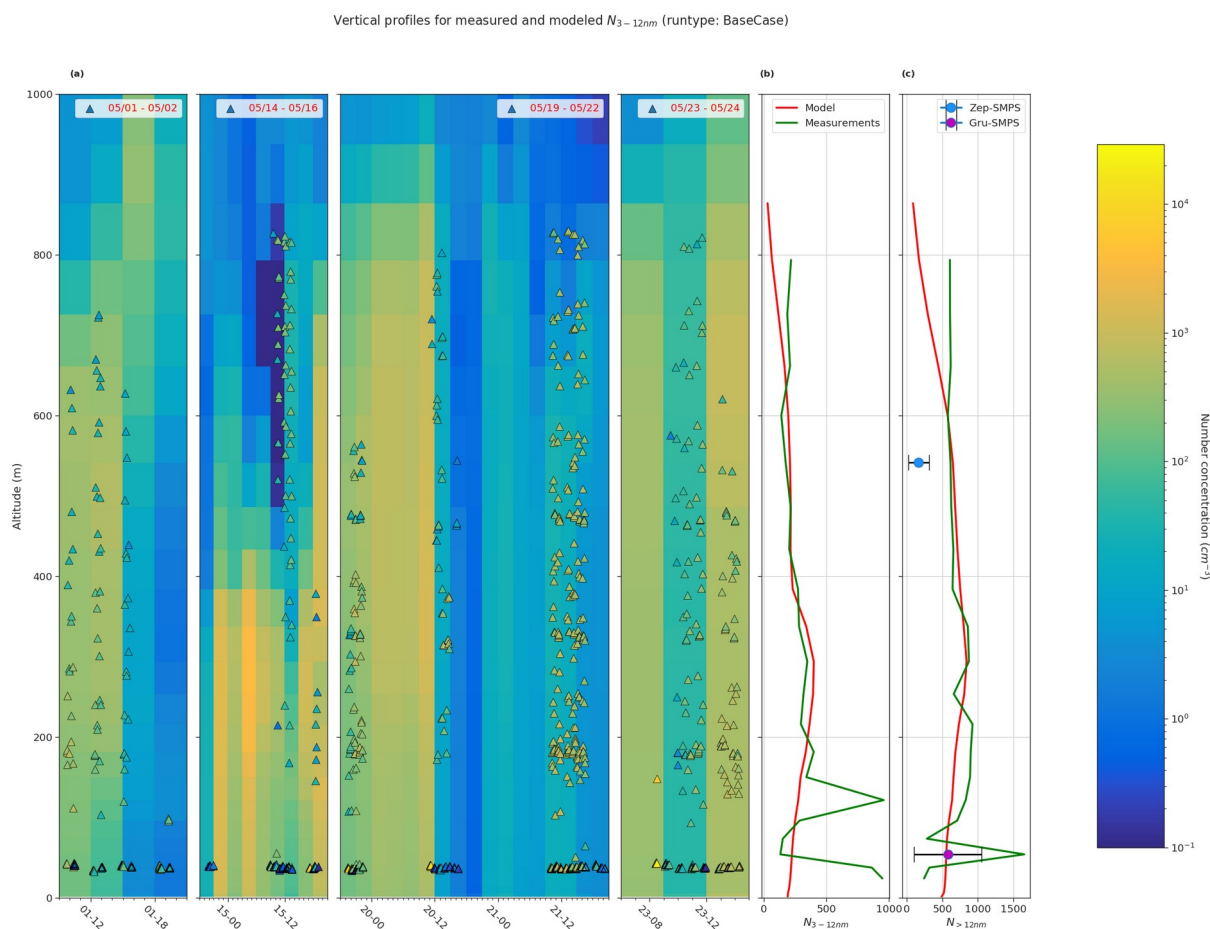
Figure 7. Comparison of vertical profiles of measured particle number concentration and *BaseCase* simulation. Panel (a) shows measured particle number concentration between 3 -12 nm ($N_{3-12\ nm}$, triangles), from CPC onboard the UAS during 4 periods 05/01- 05/02, 05/14 - 05/16, 05/19- 05/22, and 05/23- 05/24 (in legend) overlayed onto the simulated N_{3-12nm} for the same periods. Panel (b) shows the simulated and measured mean N_{3-12nm} and panel (c) show the $N_{>12nm}$ for the selected period. Additionally, Panel (c) also shows the mean SMPS particle concentrations at both Gruvebadet and Zeppelin. The horizontal bars for the mean SMPS values represent the standard deviation.

3.4 Sensitivity Tests

In this section, we will discuss the results from the sensitivity tests that we performed to complement the main *BaseCase* simulations. The settings of different sensitivity tests are described in Table 1.

Median particle size distribution for sensitivity tests

613   The sensitivity study *Cloudoff* was performed to test how in-cloud processing affects the

614   formation of larger particles, especially the accumulation mode (Figure 8). In the *Cloudoff*

615   test, in-cloud processing was switched off in the model and the RH was set to just below

616   supersaturation (99.9999%) in the model grid cell where clouds (RH=100.5%) exists in the

617   *BaseCase* runs. The aim of the *Cloudoff* simulation was to investigate if the model can

618   capture the observed accumulation mode without aerosol cloud processing. It is clear from

619   Figure 8 (a) and (b) that in *Cloudoff* simulations, the median size distribution lacks the

620   accumulation mode and Hoppel minima and has a higher Aitken mode particle concentration

621   compared to either *BaseCase* or the measured median size distribution. This further

622   emphasizes the importance of in-cloud processing in activation of particles to CCN sizes and

623   their growth to larger sizes. However, it should be noted, that other processes such as

624   Brownian scavenging by larger cloud droplets could result in the shift in particles from the

625   Aitken mode to accumulation mode (as seen in median measured size distribution, Figure 8,

626   Noble and Hudson, (2019)). Another noteworthy point in *Cloudoff* simulations is the larger

627   number concentration of particles <10 nm compared to other cases. One plausible reason is

628   the lack of activated cloud droplets, since the large surface areas of activated droplets are

629   efficient at Brownian scavenging of smaller particles (Hudson et al., 2015). Likewise, the

630   median particle number size distribution from the sensitivity tests with lower cloud

631   supersaturation (*S*) of 0.1% *SSat=0.1,* reduces the accumulation mode particles, since there

632   are fewer particles with $S_c < S$ available for activation. Increasing *S* to 0.4% increases

633   accumulation mode particles, since more particles with $S_c < S$ are activated to cloud droplets

634   (Aitken mode concentration decreases with respect to *BaseCase* simulations, since more

635   smaller particles are activated into cloud droplets). Therefore, simulated results show that

636   increasing the cloud supersaturation results in a higher number of smaller particles being

637   activated into cloud droplets and shifts the simulated Hoppel minima close to the measured

638   sizes. Figure S6, in supplementary shows median particle size distribution for all sensitivity

639   tests.

640   The *SalterSSA* sensitivity test underestimates both the Aitken and accumulation mode

641   concentrations at Gruvebadet (Figure S5, supplementary). The Salter sea-spray

642   parameterization produces ~ 2 magnitudes fewer Aitken mode particles compared to Sofiev

643   et. al, 2011, while the coarse mode particle emissions using *SalterSSA* parameterization are

644   higher than Sofiev et. al 2011. This can cause MSA, H_2SO_4 and NH_3 to partition onto coarse

645   mode particles rather than contributing to NPF and growth of the nucleation and Aitken mode

646   particles, which substantially lowers the Aitken and accumulation mode number

concentrations. The *NPFoff* simulation from Figure S6 shows lower Aitken mode concentrations, implying that the main contributor to Aitken mode particle number concentrations are the secondary aerosols rather than the primary sea-salt particles.
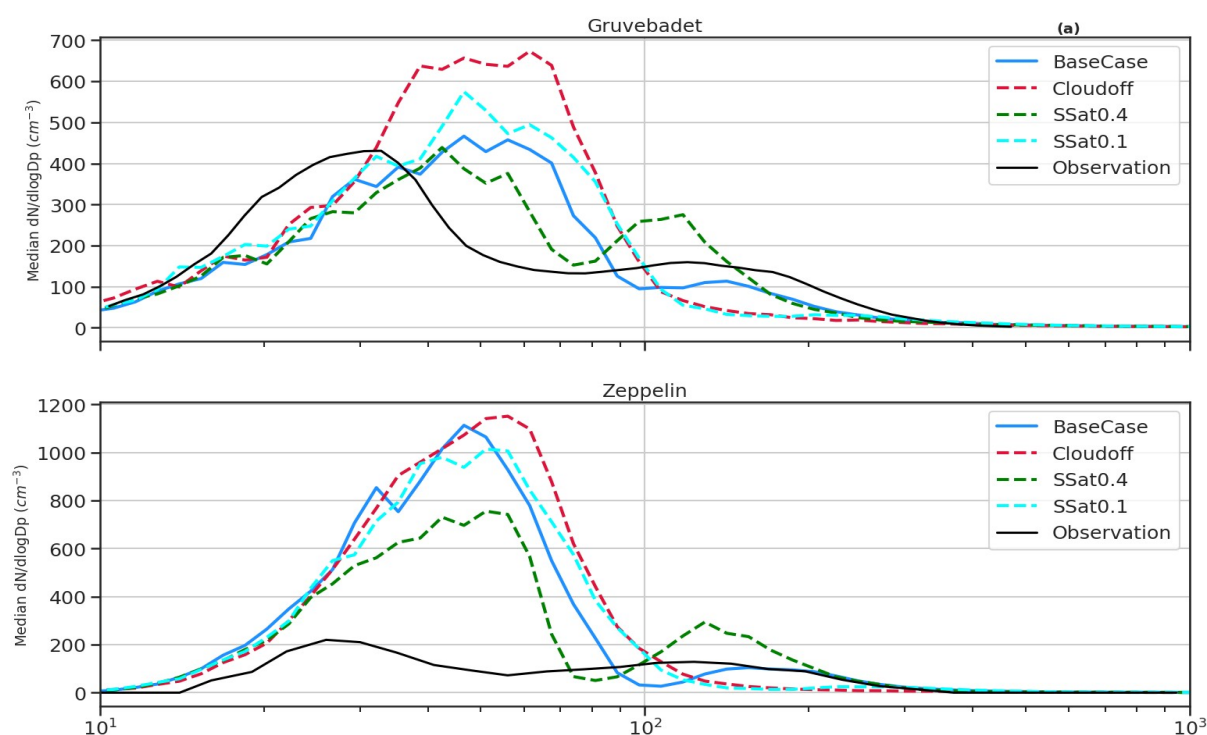
Figure 8: Median size distribution at Gruvebadet (panel (a)) and Zeppelin (panel (b)) for all the sensitivity tests *Cloudoff, SSat=0.4,* and *SSat=0.1* (colored dashed lines) including *BaseCase* (blue solid line) and observations (black solid line).

Another parameter of uncertainty is the concentration of NH_3 in the marine atmosphere. The *LowNH₃* simulations, as expected, result in lower Aitken mode particles, whereas *HighNH₃* simulations show an overprediction of Aitken mode concentrations (Figure S6, supplementary). This underlines the necessity of constraining ocean and marine emissions of NH_3 to better predict the aerosol particle formation in marine polar environments.

Particle phase comparison for sensitivity tests

Figure 9 shows the contribution of constituent compounds to PM at different particle sizes with respect to the *BaseCase* simulation. The overall mean contribution of SO_4^{2-} and MSA to total PM_{10} decreased by ~8% and 11% respectively, in *Cloudoff* runs compared to the *BaseCase* simulations. It is expected that in non-cloud conditions there is a reduction in SO_4^{2-} and MSA PM contribution because of the reduced partitioning of gaseous SO_2 to the cloud droplets (for PM SO_4^{2-} formation) and inhibition of MSIA ozonolysis in the cloud droplets

666 (leading to PM MSA formation) (Chen et al., 2018; Hoffmann et al., 2016; Wollesen de Jonge

667 et al., 2021). This is observed for accumulation mode particles between size ranges of 100 nm

668 to1 μm which is characterized by lower SO_4^{2-} and MSA PM. On the other hand, PM SO_4^{2-} and

669 MSA increase for coarse mode particles (> 1 μm). Without cloud droplet activation the

670 deliquescent sea spray coarse mode particles become a major liquid water reservoir where

671 MSIA and to a lesser extent SO_2 are dissolved and oxidized into MSA and SO_4^{2-}, which partly

672 explains the increase in PM MSA and SO_4^{2-} for sizes > 1 μm. The results from *Cloudoff*

673 simulation agrees with the findings from Wollesen de Jonge et al., 2021, who found that MSA

674 was almost exclusively formed in the aqueous phase via MSIA ozonolysis in cloud droplets

675 and deliquescent particles during and in between in-cloud periods. PM SO_4^{2-} in *Cloudoff* runs

676 is mainly driven via condensation of H_2SO_4, since an increase in SO_2 gas-phase

677 concentrations (~42% with respect to *BaseCase*) promoted gas-phase H_2SO_4 production

678 (increase of ~44% with respect to *BaseCase*), and therefore H_2SO_4 derived PM SO_4^{2-}.

679 In the *woDissolution* simulation, all the PM MSA and SO_4^{2-} are a result of the condensation of

680 $MSA_{(g)}$ and $H_2SO_{4(g)}$, since irreversible aqueous-phase chemistry is switched off. The overall

681 contribution of PM SO_4^{2-} to the total PM_{10} increases by ~12% relative to the *BaseCase* run,

682 while on the other hand, the contribution of PM MSA decreases by ~87% (relative to

683 *BaseCase*). The lower PM_{10} MSA in *woDissolution* simulation emphasizes the importance of

684 aqueous-phase formation of MSA to the growth of particles. The effect of precipitation on

685 modeled PM (*NoPrecip*) indicates an increase in PM Na^+ and Cl^- of ~112% and 119%

686 respectively, as compared to *BaseCase* (Figure S8). This is because of the decrease in the wet

687 deposition of aerosol and sea-spray particles by rain events and below cloud scavenging. The

688 consequence of neglecting precipitation results in increased condensation sink for H_2SO_4 and

689 NH_3 (increase of 62% and 22% in PM SO_4^{2-}, NH_4^+ respectively), but since sea-spray aerosols

690 are not scavenged by the wet removal process, the overall fractional contribution to PM by

691 SO_4^{2-}, NH_4^+ and MSA is lower relative to *BaseCase* runs.

692 *SalterSSA* simulation results in higher PM Cl^- and Na^+ (470% and 371% increase

693 respectively) compared to *BaseCase* runs. This is because Salter15 SSA parameterization

694 produces larger mass emission fluxes in size ranges > 1 μm compared to Sofiev11 SSA

695 parameterization (Barthel et al., 2019). Additionally, there is an increase of ~19% in PM

696 MSA, largely due to formation of MSA in larger deliquescent coarse mode particles.
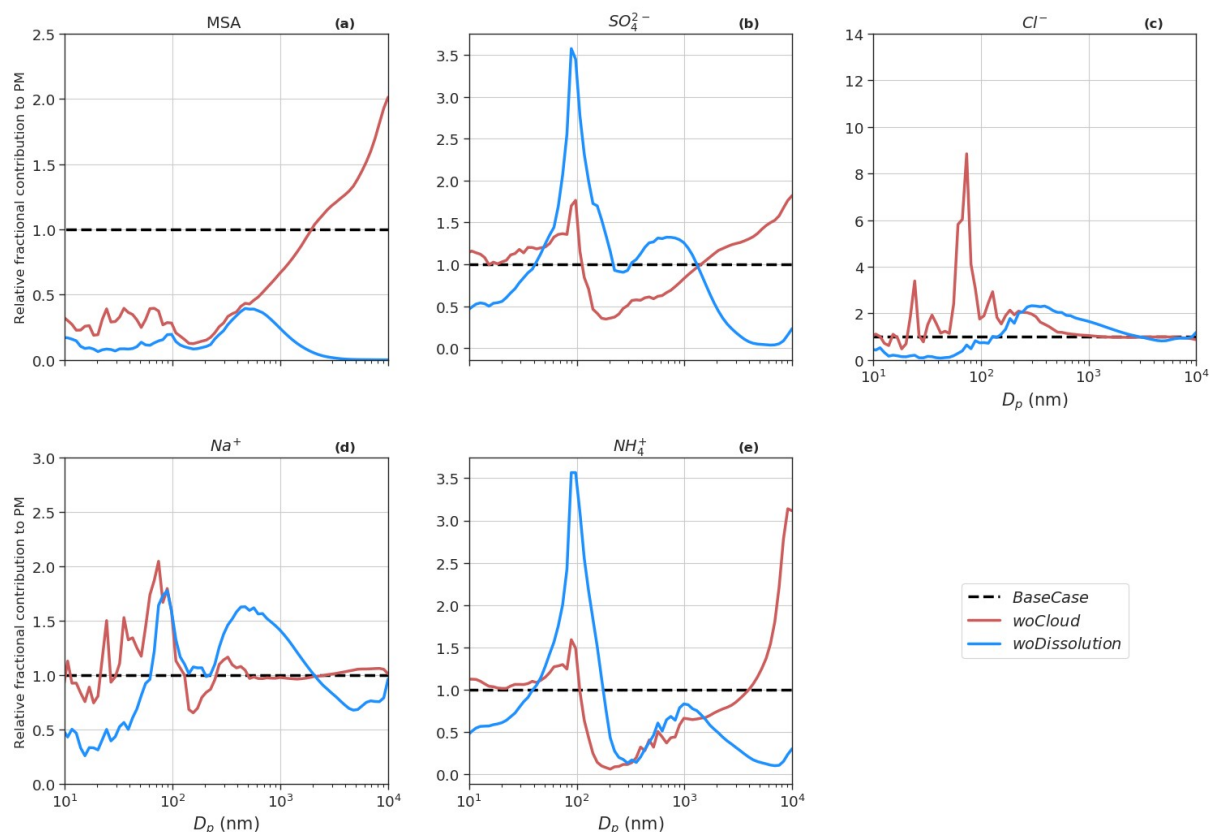
Figure 9: Contribution of constituent compounds, namely, MSA (panel (a)), SO_4^{2-} (panel (b)), Cl^- (panel(c)), Na^+ (panel (d)) and NH_4^+ (panel (e)) to PM with respect to *BaseCase* (the black dotted line).

4. Summary and conclusions

In this work, we attempt to simulate secondary aerosol formation at remote Arctic sites of Gruvebadat and Zeppelin, Ny-Ålesund, during the period of 1st - 25th of May 2018. We used the 1-dimensional column model ADCHEM which was run along FLEXPART generated Lagrangian trajectories. Since the air mass spend most of their time over the open ocean upwind of Ny-Ålesund, we use a comprehensive multi-phase DMS chemistry scheme coupled with MCMv3.3.1 and PRAM.

In the model, new particles are formed via ion-mediated H_2SO_4-NH_3 nucleation, with the initial particle growth mainly driven by condensation of H_2SO_4, while the secondary PM_{10} MSA and SO_4^{2-} contribution was mainly formed by oxidation of MSIA and SO_2 in the aqueous phase. At Gruvebadet, the modeled median particle number size distribution agrees reasonably well with the measurements, however, at Zeppelin, the simulated Aitken mode

713   median concentration is overestimated by a factor of 5.5. This relatively large discrepancy in

714   modeled and measured particle size distributions at Zeppelin, and likewise the large

715   difference between the measured particle number size distributions at Gruvebadet and

716   Zeppelin, can to a large extent be explained by the orographic effects at Zeppelin which

717   distorts the atmospheric boundary layer dynamics. Thus, while the model generally is able to

718   capture the particle number size distribution dynamics in the marine boundary layer, as

719   measured at the near sea level Gruvebadet site, it generally cannot capture the observations at

720   the mountain station of Zeppelin, which often lies above the boundary layer and may

721   experience free tropospheric conditions. This is also supported by the fact that $N_{>12\ nm}$

722   concentrations measured with the UAS above Ny-Ålesund airport agrees well with the

723   modeled particle number concentrations, at the same altitude as Zeppelin. However, both the

724   model and UAS $N_{>12nm}$ concentrations is a factor of 4 higher than the $N_{>12nm}$ observation at

725   Zeppelin.

726   Both the measured and modeled particle size distribution, at both stations, show a distinct

727   Hoppel minima, which can be explained by in-cloud processing. Model sensitivity runs with

728   varying cloud supersaturation indicate that a cloud supersaturation of 0.4% or higher is

729   required for the model to capture the observed Hoppel minima. Furthermore, model

730   sensitivity runs show that the Aitken mode particle number concentrations are dominated by

731   contribution of secondary aerosols rather than primary emissions. The modeled PM_{10} Cl^- and

732   Na^+ is positively correlated when compared to PM_{10} filter samples. The main driver for

733   secondary aerosol particle growth is the formation of MSA via aqueous phase ozonolysis of

734   the DMS oxidation product MSIA. This demonstrates the importance of multi-phase DMS

735   chemistry in capturing the size resolved secondary aerosol growth in marine polar regions.

736   The sensitivity studies indicate that it is important to limit the uncertainties in parameters such

737   as cloud supersaturation and NH_3 emissions over open oceans to get a better constraint on

738   secondary aerosol formation and its subsequent climatic effects. This work was a first attempt

739   to simulate new particle and secondary aerosol formation in marine polar regions using a

740   process based chemistry transport model that includes a comprehensive multi-phase DMS and

741   halogen chemistry mechanism, detailed gas-molecular cluster and aerosol dynamics. In future

742   studies, we aim to implement ADCHEM for extended studies in polar marine and remote

743   continental regions where different atmospheric constituents such as HIO_3, terpenes and

744   amines drive secondary aerosol formation.

745

Acknowledgments

The ALADINA study was funded by the German Research Foundation under grants LA 2907/5-3 and WI 1449/22-3. M. Sipilä acknowledges Academy of Finland (296628) and the European Research Council (ERC) under the European Union's Horizon 2020 research and innovation programme (GASPARCON, grant agreement no. 714621). This project has received funding from the Swedish Research Council Formas project no. 2018-01745-COBACCA, Swedish Research Council VR project no. 2019-05006, the Crafoord foundation through project number 20210969. The presented research has been also been funded by the Academy of Finland (Center of Excellence in Atmospheric Sciences) grant no. 4100200.

The authors would like to thank Tinja Olenius from the Swedish Meteorological and Hydrological (SMHI) for help with the implementation of ACDC in ADCHEM. We would also like to acknowledge the invaluable contribution of computational resources from CSC-IT Center for Science, Finland. The authors would like to thank Noora Hyytinen from the University of Oulu and University of Eastern Finland for providing the Henry's law coefficient and dissolution constants which were used in the multi-phase chemistry.

Observations at Zeppelin station were supported by Swedish Environmental Protection Agency (Naturvårdsverket) and by "Arctic Climate Across Scales (ACAS)" project funded by Knut and Alice Wallenberg Foundation and by project IWCAA funded by agency FORMAS. Authors would like to also thank for large support to Norwegian Polar Institute (NPI).

Author Contributions

CX, PR, MBoy, BA and BW planned and designed the study. PR, RWdJ and CX developed and setup the ADCHEM model. CX, MB and VV performed the FLEXPART model simulations. BA, BW, RoTh, and RT provided the measurement data. Resources were provided by PR and MBoy. CX, PR and MBoy wrote the original draft, which included visualizations made by CX and PR. All other authors discussed the results and contributed to the final manuscript.

Competing interests

The authors declare that they do have no conflict of interest.

References

AMAP: Snow, Water, Ice and Permafrost in the Arctic (SWIPA): Climate Change and the

778 Cryosphere. [online] Available from:
779 http://amap.no/swipa/%5Cnhttp://amap.no/swipa/CombinedReport.pdf%5Cnhttp://amap.no/
780 swipa/SWIPA2011ExecutiveSummaryV2.pdf%5Cnhttp://amap.no/swipa/
781 SwipaSimpleSummary-SEC.pdf, 2011.

782 AMAP: AMAP, 2017. Snow, Water, Ice and Permafrost in the Arctic (SWIPA) 2017. Arctic
783 Monitoring and Assessment Programme (AMAP), Oslo, Norway. xiv + 269 pp. [online]
784 Available from: https://www.amap.no/documents/doc/snow-water-ice-and-permafrost-in-the-
785 arctic-swipa-2017/1610, 2017.

786 AMAP: AMAP Arctic Climate Change Update 2021: Key Trends and Impacts, , 16 pp
787 [online] Available from: https://www.amap.no/documents/download/6759/inline, 2021.

788 Amore, A., Giardi, F., Becagli, S., Caiazzo, L., Mazzola, M., Severi, M. and Traversi, R.:
789 Source apportionment of sulphate in the High Arctic by a 10 yr-long record from Gruvebadet
790 Observatory (Ny-Ålesund, Svalbard Islands), Atmos. Environ., 270(July 2021),
791 doi:10.1016/j.atmosenv.2021.118890, 2022.

792 Arrigo, K. R. and van Dijken, G. L.: Continued increases in Arctic Ocean primary production,
793 Prog. Oceanogr., 136, 60–70, doi:10.1016/j.pocean.2015.05.002, 2015.

794 Ayers, G. P., Gillett, R. W., Cainey, J. M. and Dick, A. L.: Chloride and bromide loss from
795 sea-salt particles in Southern Ocean air, J. Atmos. Chem., 33(3), 299–319,
796 doi:10.1023/A:1006120205159, 1999.

797 Baccarini, A., Karlsson, L., Dommen, J., Duplessis, P., Vüllers, J., Brooks, I. M., Saiz-Lopez,
798 A., Salter, M., Tjernström, M., Baltensperger, U., Zieger, P. and Schmale, J.: Frequent new
799 particle formation over the high Arctic pack ice by enhanced iodine emissions, Nat.
800 Commun., 11(1), 1–11, doi:10.1038/s41467-020-18551-0, 2020.

801 Bärfuss, K., Pätzold, F., Altstädter, B., Kathe, E., Nowak, S., Bretschneider, L., Bestmann, U.
802 and Lampert, A.: New setup of the UAS ALADINA for measuring boundary layer properties,
803 atmospheric particles and solar radiation, Atmosphere (Basel)., 9(1),
804 doi:10.3390/atmos9010028, 2018.

805 Barnes, I., Hjorth, J. and Mihalapoulos, N.: Dimethyl sulfide and dimethyl sulfoxide and their
806 oxidation in the atmosphere, Chem. Rev., 106(3), 940–975, doi:10.1021/cr020529+, 2006.

807 Barrie, L. A.: Arctic air pollution: An overview of current knowledge, Atmos. Environ.,
808 20(4), 643–663, doi:10.1016/0004-6981(86)90180-0, 1986.

809 Barthel, S., Tegen, I. and Wolke, R.: Do new sea spray aerosol source functions improve the
810 results of a regional aerosol model?, Atmos. Environ., 198(May 2018), 265–278,
811 doi:10.1016/j.atmosenv.2018.10.016, 2019.

812 Beck, L. J., Sarnela, N., Junninen, H., Hoppe, C. J. M., Garmash, O., Bianchi, F., Riva, M.,
813 Rose, C., Peräkylä, O., Wimmer, D., Kausiala, O., Jokinen, T., Ahonen, L., Mikkilä, J.,
814 Hakala, J., He, X. C., Kontkanen, J., Wolf, K. K. E., Cappelletti, D., Mazzola, M., Traversi,
815 R., Petroselli, C., Viola, A. P., Vitale, V., Lange, R., Massling, A., Nøjgaard, J. K., Krejci, R.,

816 Karlsson, L., Zieger, P., Jang, S., Lee, K., Vakkari, V., Lampilahti, J., Thakur, R. C., Leino,
817 K., Kangasluoma, J., Duplissy, E. M., Siivola, E., Marbouti, M., Tham, Y. J., Saiz-Lopez, A.,
818 Petäjä, T., Ehn, M., Worsnop, D. R., Skov, H., Kulmala, M., Kerminen, V. M. and Sipilä, M.:
819 Differing Mechanisms of New Particle Formation at Two Arctic Sites, Geophys. Res. Lett.,
820 48(4), 1–11, doi:10.1029/2020GL091334, 2021.

821 Bengtsson, L., Hodges, K. I., Koumoutsaris, S., Zahn, M. and Berrisford, P.: The changing
822 energy balance of the polar regions in a warmer climate, J. Clim., 26(10), 3112–3129,
823 doi:10.1175/JCLI-D-12-00233.1, 2013.

824 Berndt, T., Chen, J., Møller, K. H., Hyttinen, N., Prisle, N. L., Tilgner, A., Hoffmann, E. H.,
825 Herrmann, H. and Kjaergaard, H. G.: SO2formation and peroxy radical isomerization in the
826 atmospheric reaction of OH radicals with dimethyl disulfide, Chem. Commun., 56(88),
827 13634–13637, doi:10.1039/d0cc05783e, 2020.

828 Bräuer, P., Tilgner, A., Wolke, R. and Herrmann, H.: Mechanism development and modelling
829 of tropospheric multiphase halogen chemistry: The CAPRAM Halogen Module 2.0 (HM2), J.
830 Atmos. Chem., 70(1), 19–52, doi:10.1007/s10874-013-9249-6, 2013.

831 Campolongo, F., Saltelli, A., Jensen, N. R., Wilson, J. and Hjorth, J.: The role of multiphase
832 chemistry in the oxidation of dimethylsulphide (DMS). A latitude dependent analysis, J.
833 Atmos. Chem., 32(3), 327–356, doi:10.1023/A:1006154618511, 1999.

834 Chen, Q., Sherwen, T., Evans, M. and Alexander, B.: DMS oxidation and sulfur aerosol
835 formation in the marine troposphere: A focus on reactive halogen and multiphase chemistry,
836 Atmos. Chem. Phys., 18(18), 13617–13637, doi:10.5194/acp-18-13617-2018, 2018.

837 Clarke, A. D., Owens, S. R. and Zhou, J.: An ultrafine sea-salt flux from breaking waves:
838 Implications for cloud condensation nuclei in the remote marine atmosphere, J. Geophys. Res.
839 Atmos., 111(6), doi:10.1029/2005JD006565, 2006.

840 Cuevas, C. A., Maffezzoli, N., Corella, J. P., Spolaor, A., Vallelonga, P., Kjær, H. A.,
841 Simonsen, M., Winstrup, M., Vinther, B., Horvat, C., Fernandez, R. P., Kinnison, D.,
842 Lamarque, J. F., Barbante, C. and Saiz-Lopez, A.: Rapid increase in atmospheric iodine levels
843 in the North Atlantic since the mid-20th century, Nat. Commun., 9(1), 1–6,
844 doi:10.1038/s41467-018-03756-1, 2018.

845 Dall'osto, M., Beddows, D. C. S., Tunved, P., Harrison, R. M., Lupi, A., Vitale, V., Becagli,
846 S., Traversi, R., Park, K. T., Jun Yoon, Y., Massling, A., Skov, H., Lange, R., Strom, J. and
847 Krejci, R.: Simultaneous measurements of aerosol size distributions at three sites in the
848 European high Arctic, Atmos. Chem. Phys., 19(11), 7377–7395, doi:10.5194/acp-19-7377-
849 2019, 2019a.

850 Dall'osto, M., Beddows, D. C. S., Tunved, P., Harrison, R. M., Lupi, A., Vitale, V., Becagli,
851 S., Traversi, R., Park, K. T., Jun Yoon, Y., Massling, A., Skov, H., Lange, R., Strom, J. and
852 Krejci, R.: Simultaneous measurements of aerosol size distributions at three sites in the
853 European high Arctic, Atmos. Chem. Phys., 19(11), 7377–7395, doi:10.5194/acp-19-7377-
854 2019, 2019b.

855   Dall'Osto, M., Ovadnevaite, J., Paglione, M., Beddows, D. C. S., Ceburnis, D., Cree, C.,
856   Cortés, P., Zamanillo, M., Nunes, S. O., Pérez, G. L., Ortega-Retuerta, E., Emelianov, M.,
857   Vaqué, D., Marrasé, C., Estrada, M., Sala, M. M., Vidal, M., Fitzsimons, M. F., Beale, R.,
858   Airs, R., Rinaldi, M., Decesari, S., Facchini, M. C., Harrison, R. M., O'Dowd, C. and Simó,
859   R.: Antarctic sea ice region as a source of biogenic organic nitrogen in aerosols, Sci. Rep.,
860   7(1), 1–10, doi:10.1038/s41598-017-06188-x, 2017a.

861   Dall'Osto, M., Beddows, D. C. S., Tunved, P., Krejci, R., Ström, J., Hansson, H. C., Yoon, Y.
862   J., Park, K. T., Becagli, S., Udisti, R., Onasch, T., Ódowd, C. D., Simó, R. and Harrison, R.
863   M.: Arctic sea ice melt leads to atmospheric new particle formation, Sci. Rep., 7(1), 1–10,
864   doi:10.1038/s41598-017-03328-1, 2017b.

865   Damian, V., Sandu, A., Damian, M., Potra, F. and Carmichael, G. R.: The kinetic
866   preprocessor KPP - A software environment for solving chemical kinetics, Comput. Chem.
867   Eng., 26(11), 1567–1579, doi:10.1016/S0098-1354(02)00128-X, 2002.

868   Feingold, G. and Kreidenweis, S.: Does cloud processing of aerosol enhance droplet
869   concentrations?, J. Geophys. Res. Atmos., 105(D19), 24351–24361,
870   doi:10.1029/2000JD900369, 2000.

871   Flossmann, A. I. and Wobrock, W.: Cloud processing of aerosol particles in marine
872   stratocumulus clouds, Atmosphere (Basel)., 10(9), doi:10.3390/atmos10090520, 2019.

873   Fossum, K. N., Ovadnevaite, J., Ceburnis, D., Dall'Osto, M., Marullo, S., Bellacicco, M.,
874   Simó, R., Liu, D., Flynn, M., Zuend, A. and O'Dowd, C.: Summertime Primary and
875   Secondary Contributions to Southern Ocean Cloud Condensation Nuclei, Sci. Rep., 8(1), 1–
876   14, doi:10.1038/s41598-018-32047-4, 2018.

877   Frey, M. M., Norris, S. J., Brooks, I. M., Anderson, P. S., Nishimura, K., Yang, X., Jones, A.
878   E., Nerentorp Mastromonaco, M. G., Jones, D. H. and Wolff, E. W.: First direct observation
879   of sea salt aerosol production from blowing snow above sea ice, Atmos. Chem. Phys., 20(4),
880   2549–2578, doi:10.5194/acp-20-2549-2020, 2020.

881   Gantt, B., He, J., Zhang, X., Zhang, Y. and Nenes, A.: Incorporation of advanced aerosol
882   activation treatments into CESM/CAM5: Model evaluation and impacts on aerosol indirect
883   effects, Atmos. Chem. Phys., 14(14), 7485–7497, doi:10.5194/acp-14-7485-2014, 2014.

884   Granier, C., Darras, S., Gon, H. D. van der, Jana, D., Elguindi, N., Bo, G., Michael, G., Marc,
885   G., Jalkanen, J.-P., Kuenen, J., Liousse, C., Quack, B., Simpson, D. and Sindelarova, K.: The
886   Copernicus Atmosphere Monitoring Service global and regional emissions (April 2019
887   version), , (April) [online] Available from: https://hal.archives-ouvertes.fr/hal-
888   02322431%0Ahttps://hal.archives-ouvertes.fr/hal-02322431/document, 2019.

889   Guenther, A., Karl, T., Harley, P., Weidinmyer, C., Palmer, P. I. and Geron, C.: Edinburgh
890   Research Explorer Estimates of global terrestrial isoprene emissions using MEGAN (Model
891   of Emissions of Gases and Aerosols from Nature) and Physics Estimates of global terrestrial
892   isoprene emissions using MEGAN (Model of Emissions of Gases an, Atmos. Chem. Phys.,
893   (6), 3181–3210, 2006.

Herenz, P., Wex, H., Henning, S., Kristensen, T. B., Rubach, F., Roth, A., Borrmann, S., Bozem, H., Schulz, H. and Stratmann, F.: Measurements of aerosol and CCN properties in the Mackenzie River delta (Canadian Arctic) during spring--summer transition in May 2014, Atmos. Chem. Phys., 18(7), 4477–4496, doi:10.5194/acp-18-4477-2018, 2018.

Hertel, O., Christensen, J. and Hov, Ø.: Modelling of the end products of the chemical decomposition of DMS in the marine boundary layer, Atmos. Environ., 28(15), 2431–2449, doi:10.1016/1352-2310(94)90395-6, 1994.

Hodshire, A. L., Campuzano-Jost, P., Kodros, J. K., Croft, B., Nault, B. A., Schroder, J. C., Jimenez, J. L. and Pierce, J. R.: The potential role of methanesulfonic acid (MSA) in aerosol formation and growth and the associated radiative forcings, Atmos. Chem. Phys., 19(5), 3137–3160, doi:10.5194/acp-19-3137-2019, 2019.

Hoffmann, E. H., Tilgner, A., Schrödner, R., Bräuer, P., Wolke, R. and Herrmann, H.: An advanced modeling study on the impacts and atmospheric implications of multiphase dimethyl sulfide chemistry, Proc. Natl. Acad. Sci. U. S. A., 113(42), 11776–11781, doi:10.1073/pnas.1606320113, 2016.

Hoose, C., Lohmann, U., Bennartz, R., Croft, B. and Lesins, G.: Global simulations of aerosol processing in clouds, Atmos. Chem. Phys., 8(23), 6939–6963, doi:10.5194/acp-8-6939-2008, 2008.

Hoppel, W. A. and Frick, G. M.: Submicron aerosol size distributions measured over the tropical and South Pacific, Atmos. Environ. Part A, Gen. Top., 24(3), 645–659, doi:10.1016/0960-1686(90)90020-N, 1990.

Hoppel, W. A., Fitzgerald, J. W. and Larson, R. E.: Aerosol size distributions in air masses advecting off the east coast of the United States., J. Geophys. Res., 90(D1), 2365–2379, doi:10.1029/JD090iD01p02365, 1985.

Hoppel, W. A., Frick, G. M. and Larson, R. E.: Effect of nonprecipitating clouds on the aerosol size distribution in the marine boundary layer, Geophys. Res. Lett., 13, 125–128, 1986.

Hudson, J. G., Noble, S. and Tabor, S.: Cloud supersaturations from CCN spectra Hoppel minima, J. Geophys. Res., 120(8), 3436–3452, doi:10.1002/2014JD022669, 2015.

Jang, S., Park, K. T., Lee, K., Yoon, Y. J., Kim, K., Chung, H. Y., Jang, E., Becagli, S., Lee, B. Y., Traversi, R., Eleftheriadis, K., Krejci, R. and Hermansen, O.: Large seasonal and interannual variations of biogenic sulfur compounds in the Arctic atmosphere (Svalbard; 78.9g N, 11.9g E), Atmos. Chem. Phys., 21(12), 9761–9777, doi:10.5194/acp-21-9761-2021, 2021.

Jenkin, M. E., Saunders, S. M. and Pilling, M. J.: The tropospheric degradation of volatile organic compounds: A protocol for mechanism development, Atmos. Environ., 31(1), 81–104, doi:10.1016/S1352-2310(96)00105-7, 1997.

Jenkin, M. E., Young, J. C. and Rickard, A. R.: The MCM v3.3.1 degradation scheme for

932   isoprene, Atmos. Chem. Phys., 15(20), 11433–11459, doi:10.5194/acp-15-11433-2015, 2015.

933   Jeričević, A., Kraljević, L., Grisogono, B., Fagerli, H. and Večenaj, Ž.: Parameterization of
934   vertical diffusion and the atmospheric boundary layer height determination in the EMEP
935   model, Atmos. Chem. Phys., 10(2), 341–364, doi:10.5194/acp-10-341-2010, 2010.

936   Jokinen, T., Sipilä, M., Kontkanen, J., Vakkari, V., Tisler, P., Duplissy, E. M., Junninen, H.,
937   Kangasluoma, J., Manninen, H. E., Petäjä, T., Kulmala, M., Worsnop, D. R., Kirkby, J.,
938   Virkkula, A. and Kerminen, V. M.: Ion-induced sulfuric acid–ammonia nucleation drives
939   particle formation in coastal Antarctica, Sci. Adv., 4(11), 1–7, doi:10.1126/sciadv.aat9744,
940   2018.

941   Kettle, A. J. and Andreae, M. O.: Flux of dimethylsulfide from the oceans: A comparison of
942   updated data sets and flux models, J. Geophys. Res. Atmos., 105(D22), 26793–26808,
943   doi:10.1029/2000JD900252, 2000.

944   Kim, I., Zhang, M., Kim, K. and Park, K.: First high-frequency underway observation of dms
945   distribution in the southern ocean during austral autumn, Atmosphere (Basel)., 12(1), 1–10,
946   doi:10.3390/atmos12010122, 2021.

947   Kirkby, J., Duplissy, J., Sengupta, K., Frege, C., Gordon, H., Williamson, C., Heinritzi, M.,
948   Simon, M., Yan, C., Almeida, J., Trostl, J., Nieminen, T., Ortega, I. K., Wagner, R., Adamov,
949   A., Amorim, A., Bernhammer, A. K., Bianchi, F., Breitenlechner, M., Brilke, S., Chen, X.,
950   Craven, J., Dias, A., Ehrhart, S., Flagan, R. C., Franchin, A., Fuchs, C., Guida, R., Hakala, J.,
951   Hoyle, C. R., Jokinen, T., Junninen, H., Kangasluoma, J., Kim, J., Krapf, M., Kurten, A.,
952   Laaksonen, A., Lehtipalo, K., Makhmutov, V., Mathot, S., Molteni, U., Onnela, A., Perakyla,
953   O., Piel, F., Petaja, T., Praplan, A. P., Pringle, K., Rap, A., Richards, N. A. D., Riipinen, I.,
954   Rissanen, M. P., Rondo, L., Sarnela, N., Schobesberger, S., Scott, C. E., Seinfeld, J. H.,
955   Sipila, M., Steiner, G., Stozhkov, Y., Stratmann, F., Tomé, A., Virtanen, A., Vogel, A. L.,
956   Wagner, A. C., Wagner, P. E., Weingartner, E., Wimmer, D., Winkler, P. M., Ye, P., Zhang,
957   X., Hansel, A., Dommen, J., Donahue, N. M., Worsnop, D. R., Baltensperger, U., Kulmala,
958   M., Carslaw, K. S. and Curtius, J.: Ion-induced nucleation of pure biogenic particles, Nature,
959   533(7604), 521–526, doi:10.1038/nature17953, 2016.

960   Kloster, S., Feichter, J., Maier-Reimer, E., Six, K. D., Stier, P. and Wetzel, P.: DMS cycle in
961   the marine ocean-atmosphere system - A global model study, Biogeosciences, 3(1), 29–51,
962   doi:10.5194/bg-3-29-2006, 2006.

963   Lampert, A., Altstädter, B., Bärfuss, K., Bretschneider, L., Sandgaard, J., Michaelis, J.,
964   Lobitz, L., Asmussen, M., Damm, E., Käthner, R., Krüger, T., Lüpkes, C., Nowak, S., Peuker,
965   A., Rausch, T., Reiser, F., Scholtz, A., Sotomayor-Zakharov, D., Gaus, D., Bansmer, S.,
966   Wehner, B. and Pätzold, F.: Unmanned aerial systems for investigating the polar atmospheric
967   boundary layer-technical challenges and examples of applications, Atmosphere (Basel).,
968   11(4), doi:10.3390/ATMOS11040416, 2020.

969   Lana, A., Bell, T. G., Simó, R., Vallina, S. M., Ballabrera-Poy, J., Kettle, A. J., Dachs, J.,
970   Bopp, L., Saltzman, E. S., Stefels, J., Johnson, J. E. and Liss, P. S.: An updated climatology

971 of surface dimethlysulfide concentrations and emission fluxes in the global ocean, Global
972 Biogeochem. Cycles, 25(1), 1–17, doi:10.1029/2010GB003850, 2011.

973 Lee, H., Lee, K., Lunder, C. R., Krejci, R., Aas, W., Park, J., Park, K.-T., Lee, B. Y., Yoon,
974 Y. J. and Park, K.: Atmospheric new particle formation characteristics in the Arctic as
975 measured at Mount Zeppelin, Svalbard, from 2016 to 2018, Atmos. Chem. Phys., 20(21),
976 13425–13441, doi:10.5194/acp-20-13425-2020, 2020..

977 Lenssen, N. J. L., Schmidt, G. A., Hansen, J. E., Menne, M. J., Persin, A., Ruedy, R. and
978 Zyss, D.: Improvements in the GISTEMP Uncertainty Model, J. Geophys. Res. Atmos.,
979 124(12), 6307–6326, doi:10.1029/2018JD029522, 2019.

980 Lupi, A., Busetto, M., Becagli, S., Giardi, F., Lanconelli, C., Mazzola, M., Udisti, R.,
981 Hansson, H. C., Henning, T., Petkov, B., Ström, J., Krejci, R., Tunved, P., Viola, A. Pietro
982 and Vitale, V.: Multi-seasonal ultrafine aerosol particle number concentration measurements
983 at the Gruvebadet observatory, Ny-Ålesund, Svalbard Islands, Rend. Lincei, 27, 59–71,
984 doi:10.1007/s12210-016-0532-8, 2016.

985 Mårtensson, E. M., Nilsson, E. D., de Leeuw, G., Cohen, L. H. and Hansson, H.-C.:
986 Laboratory simulations and parameterization of the primary marine aerosol production, J.
987 Geophys. Res. Atmos., 108(D9), doi:https://doi.org/10.1029/2002JD002263, 2003.

988 Mikkola, J.: Slope and valley winds in the Himalayas as simulated by the Weather Research
989 and Forecasting model, , 42, 2020.

990 Monahan, E. C., Spiel, D. E. and Davidson, K. L.: A Model of Marine Aerosol Generation
991 Via Whitecaps and Wave Disruption, in Oceanic Whitecaps: And Their Role in Air-Sea
992 Exchange Processes, edited by E. C. Monahan and G. Mac Niocaill, pp. 167–174, Springer
993 Netherlands, Dordrecht., 1986.

994 Moroni, B., Ritter, C., Crocchianti, S., Markowicz, K., Mazzola, M., Becagli, S., Traversi, R.,
995 Krejci, R., Tunved, P. and Cappelletti, D.: Individual Particle Characteristics, Optical
996 Properties and Evolution of an Extreme Long-Range Transported Biomass Burning Event in
997 the European Arctic (Ny-Ålesund, Svalbard Islands), J. Geophys. Res. Atmos., 125(5), 1–17,
998 doi:10.1029/2019JD031535, 2020.

999 Nightingale, P. D., Liss, P. S. and Schlosser, P.: Measurements of air-sea gas transfer during
1000 an open ocean algal bloom, Geophys. Res. Lett., 27(14), 2117–2120,
1001 doi:10.1029/2000GL011541, 2000.

1002 Noble, S. and Hudson, J. G.: Cloud supersaturations and Hoppel minima, AIP Conf. Proc.,
1003 1527(September), 706–709, doi:10.1063/1.4803368, 2013.

1004 Noble, S. R. and Hudson, J. G.: Effects of Continental Clouds on Surface Aitken and
1005 Accumulation Modes, J. Geophys. Res. Atmos., 124(10), 5479–5502,
1006 doi:10.1029/2019JD030297, 2019.

1007 Olenius, T., Kupiainen-Määttä, O., Ortega, I. K., Kurtén, T. and Vehkamäki, H.: Free energy
1008 barrier in the growth of sulfuric acid-ammonia and sulfuric acid-dimethylamine clusters, J.

1009 Chem. Phys., 139(8), doi:10.1063/1.4819024, 2013.

1010 Oshima, N., Yukimoto, S., Deushi, M., Koshiro, T., Kawai, H., Tanaka, T. Y. and Yoshida,
1011 K.: Global and Arctic effective radiative forcing of anthropogenic gases and aerosols in MRI-
1012 ESM2.0, Prog. Earth Planet. Sci., 7(1), doi:10.1186/s40645-020-00348-w, 2020.

1013 Öström, E., Putian, Z., Schurgers, G., Mishurov, M., Kivekäs, N., Lihavainen, H., Ehn, M.,
1014 Rissanen, M. P., Kurtén, T., Boy, M., Swietlicki, E. and Roldin, P.: Modeling the role of
1015 highly oxidized multifunctional organic molecules for the growth of new particles over the
1016 boreal forest region, Atmos. Chem. Phys., 17(14), 8887–8901, doi:10.5194/acp-17-8887-
1017 2017, 2017.

1018 Park, K. T., Jang, S., Lee, K., Yoon, Y. J., Kim, M. S., Park, K., Cho, H. J., Kang, J. H.,
1019 Udisti, R., Lee, B. Y. and Shin, K. H.: Observational evidence for the formation of DMS-
1020 derived aerosols during Arctic phytoplankton blooms, Atmos. Chem. Phys., 17(15), 9665–
1021 9675, doi:10.5194/acp-17-9665-2017, 2017.

1022 Park, K. T., Yoon, Y. J., Lee, K., Tunved, P., Krejci, R., Ström, J., Jang, E., Kang, H. J., Jang,
1023 S., Park, J., Lee, B. Y., Traversi, R., Becagli, S. and Hermansen, O.: Dimethyl Sulfide-
1024 Induced Increase in Cloud Condensation Nuclei in the Arctic Atmosphere, Global
1025 Biogeochem. Cycles, 35(7), 1–15, doi:10.1029/2021GB006969, 2021.

1026 Paulot, F., Jacob, D. J., Johnson, M. T., Bell, T. G., Baker, A. R., Keene, W. C., Lima, I. D.,
1027 Doney, S. C. and Stock, C. A.: Global oceanic emission of ammonia: Constraints from
1028 seawater and atmospheric observations, Global Biogeochem. Cycles, 29(8), 1165–1178,
1029 doi:10.1002/2015GB005106, 2015.

1030 Petäjä, T., Duplissy, E., Tabakova, K., Schmale, J., Altstädter, B. and Ancellet, G.: Overview:
1031 Integrative and Comprehensive Understanding on Polar Environments (iCUPE) – concept
1032 and initial results, , 8551–8592, 2020.

1033 Pisso, I., Sollum, E., Grythe, H., Kristiansen, N., Cassiani, M., Eckhardt, S., Arnold, D.,
1034 Morton, D., Thompson, R., Groot Zwaaftink, C., Evangeliou, N., Sodemann, H., Haimberger,
1035 L., Henne, S., Brunner, D., Burkhart, J., Fouilloux, A., Brioude, J., Philipp, A., Seibert, P. and
1036 Stohl, A.: The Lagrangian particle dispersion model FLEXPART version 10.3, Geosci. Model
1037 Dev. Discuss., (January), 1–67, doi:10.5194/gmd-2018-333, 2019.

1038 Platt, S. M., Hov, Ø., Berg, T., Breivik, K., Eckhardt, S., Hansson, H., Heintzenberg, J.,
1039 Hermansen, O., Heslin-rees, D. and Holmén, K.: Atmospheric composition in the European
1040 Arctic and 30 years of the Zeppelin Observatory , Ny-Ålesund, , 3321–3369, 2022.

1041 Quinn, P. K., Coffman, D. J., Johnson, J. E., Upchurch, L. M. and Bates, T. S.: Small fraction
1042 of marine cloud condensation nuclei made up of sea spray aerosol, Nat. Geosci., 10(9), 674–
1043 679, doi:10.1038/ngeo3003, 2017.

1044 Rader, F., Traversi, R., Severi, M., Becagli, S., Müller, K.-J., Nakoudi, K. and Ritter, C.:
1045 Overview of Aerosol Properties in the European Arctic in Spring 2019 Based on In Situ
1046 Measurements and Lidar Data, Atmosphere (Basel)., 12(2), doi:10.3390/atmos12020271,
1047 2021.

Riddick, S. N., Dragosits, U., Blackall, T. D., Daunt, F., Wanless, S. and Sutton, M. A.: The global distribution of ammonia emissions from seabird colonies, Atmos. Environ., 55, 319–327, doi:10.1016/j.atmosenv.2012.02.052, 2012.

Roldin, P., Swietlicki, E., Schurgers, G., Arneth, A., Lehtinen, K. E. J., Boy, M. and Kulmala, M.: Development and evaluation of the aerosol dynamics and gas phase chemistry model ADCHEM, Atmos. Chem. Phys., 11(12), 5867–5896, doi:10.5194/acp-11-5867-2011, 2011.

Roldin, P., Ehn, M., Kurtén, T., Olenius, T., Rissanen, M. P., Sarnela, N., Elm, J., Rantala, P., Hao, L., Hyttinen, N., Heikkinen, L., Worsnop, D. R., Pichelstorfer, L., Xavier, C., Clusius, P., Öström, E., Petäjä, T., Kulmala, M., Vehkamäki, H., Virtanen, A., Riipinen, I. and Boy, M.: The role of highly oxygenated organic molecules in the Boreal aerosol-cloud-climate system, Nat. Commun., 10(2019), 4370, doi:10.1038/s41467-019-12338-8, 2019.

Rosati, B., Christiansen, S., Wollesen de Jonge, R., Roldin, P., Jensen, M. M., Wang, K., Moosakutty, S. P., Thomsen, D., Salomonsen, C., Hyttinen, N., Elm, J., Feilberg, A., Glasius, M. and Bilde, M.: New Particle Formation and Growth from Dimethyl Sulfide Oxidation by Hydroxyl Radicals, ACS Earth Sp. Chem., acsearthspacechem.0c00333, doi:10.1021/acsearthspacechem.0c00333, 2021.

Rosenfeld, D., Andreae, M. O., Asmi, A., Chin, M., de Leeuw, G., Donovan, D. P., Kahn, R., Kinne, S., Kivekäs, N., Kulmala, M., Lau, W., Schmidt, K. S., Suni, T., Wagner, T., Wild, M. and Quaas, J.: Global observations of aerosol-cloud-precipitation-climate interactions, Rev. Geophys., 52(4), 750–808, doi:10.1002/2013RG000441, 2014.

Salter, M. E., Zieger, P., Acosta Navarro, J. C., Grythe, H., Kirkevåg, A., Rosati, B., Riipinen, I. and Nilsson, E. D.: An empirically derived inorganic sea spray source function incorporating sea surface temperature, Atmos. Chem. Phys., 15(19), 11047–11066, doi:10.5194/acp-15-11047-2015, 2015.

Saunders, S. M., Jenkin, M. E., Derwent, R. G. and Pilling, M. J.: Protocol for the development of the Master Chemical Mechanism, MCM v3 (Part A): Tropospheric degradation of non-aromatic volatile organic compounds, Atmos. Chem. Phys., 3(1), 161–180, doi:10.5194/acp-3-161-2003, 2003.

Schemann, V. and Ebell, K.: Simulation of mixed-phase clouds with the ICON large-eddy model in the complex Arctic environment around Ny-Ålesund, Atmos. Chem. Phys., 20(1), 475–485, doi:10.5194/acp-20-475-2020, 2020.

Scott, C. E., Rap, A., Spracklen, D. V., Forster, P. M., Carslaw, K. S., Mann, G. W., Pringle, K. J., Kivekäs, N., Kulmala, M., Lihavainen, H. and Tunved, P.: The direct and indirect radiative effects of biogenic secondary organic aerosol, Atmos. Chem. Phys., 14(1), 447–470, doi:10.5194/acp-14-447-2014, 2014.

Sofiev, M., Soares, J., Prank, M., De Leeuw, G. and Kukkonen, J.: A regional-to-global model of emission and transport of sea salt particles in the atmosphere, J. Geophys. Res. Atmos., 116(21), doi:10.1029/2010JD014713, 2011.

Stock, C. A., Dunne, J. P. and John, J. G.: Global-scale carbon and energy flows through the

1087   marine planktonic food web: An analysis with a coupled physical–biological model, Prog.
1088   Oceanogr., 120, 1–28, doi:https://doi.org/10.1016/j.pocean.2013.07.001, 2014.

1089   Stohl, A., Sodemann, H., Eckhardt, S., Frank, A., Seibert, P. and Wotawa, G.: The Lagrangian
1090   particle dispersion model FLEXPART version 8 .2, 2005.

1091   Ström, J., Engvall, A. C., Delbart, F., Krejci, R. and Treffeisen, R.: On small particles in the
1092   Arctic summer boundary layer: Observations at two different heights near Ny-Ålesund,
1093   Svalbard, Tellus, Ser. B Chem. Phys. Meteorol., 61 B(2), 473–482, doi:10.1111/j.1600-
1094   0889.2008.00412.x, 2009.

1095   Traversi, R., Becagli, S., Severi, M., Caiazzo, L., Mazzola, M., Lupi, A., Fiebig, M.,
1096   Hermansen, O., Krejci, R. and Unit, A. S.: Arctic haze in a climate changing world: the 2010-
1097   2020 trend (HAZECLIC) 4, , (0000), 104–117, 2020.

1098   Tunved, P., Ström, J. and Krejci, R.: Arctic aerosol life cycle: Linking aerosol size
1099   distributions observed between 2000 and 2010 with air mass transport and precipitation at
1100   Zeppelin station, Ny-Ålesund, Svalbard, Atmos. Chem. Phys., 13(7), 3643–3660,
1101   doi:10.5194/acp-13-3643-2013, 2013.

1102   Uhlig, C., Damm, E., Peeken, I., Krumpen, T., Rabe, B., Korhonen, M. and Ludwichowski,
1103   K. U.: Sea ice and water mass influence dimethylsulfide concentrations in the central arctic
1104   ocean, Front. Earth Sci., 7(July), 1–15, doi:10.3389/feart.2019.00179, 2019.

1105   Wainwright, C. D., Pierce, J. R., Liggio, J., Strawbridge, K. B., MacDonald, A. M. and
1106   Leaitch, R. W.: The effect of model spatial resolution on Secondary Organic Aerosol
1107   predictions: A case study at Whistler, BC, Canada, Atmos. Chem. Phys., 12(22), 10911–
1108   10923, doi:10.5194/acp-12-10911-2012, 2012.

1109   Wentworth, G. R., Murphy, J. G., Croft, B., Martin, R. V., Pierce, J. R., Côté, J. S.,
1110   Courchesne, I., Tremblay, J. É., Gagnon, J., Thomas, J. L., Sharma, S., Toom-Sauntry, D.,
1111   Chivulescu, A., Levasseur, M. and Abbatt, J. P. D.: Ammonia in the summertime Arctic
1112   marine boundary layer: Sources, sinks, and implications, Atmos. Chem. Phys., 16(4), 1937–
1113   1953, doi:10.5194/acp-16-1937-2016, 2016.

1114   Wollesen de Jonge, R.: Supplement of Secondary aerosol formation from dimethyl sulfide –
1115   improved mechanis- tic understanding based on smog chamber experiments and modelling, ,
1116   9955–9976, 2021.

1117   Wollesen de Jonge, R., Elm, J., Rosati, B., Christiansen, S., Hyttinen, N., Lüdemann, D.,
1118   Bilde, M. and Roldin, P.: Secondary aerosol formation from dimethyl sulfide – improved
1119   mechanistic understanding based on smog chamber experiments and modelling, Atmos.
1120   Chem. Phys., 1–33, doi:10.5194/acp-2020-1324, 2021.

1121   Xavier, C., Rusanen, A., Zhou, P., Dean, C., Pichelstorfer, L., Roldin, P. and Boy, M.:
1122   Aerosol mass yields of selected biogenic volatile organic compounds – a theoretical study
1123   with nearly explicit gas-phase chemistry, Atmos. Chem. Phys., 19(22), 13741–13758,
1124   doi:10.5194/acp-19-13741-2019, 2019.

1125 Zheng, G., Wang, Y., Aiken, A. C., Gallo, F., Jensen, M. P., Kollias, P., Kuang, C., Luke, E.,
1126 Springston, S., Uin, J., Wood, R. and Wang, J.: Marine boundary layer aerosol in the eastern
1127 North Atlantic: Seasonal variations and key controlling processes, Atmos. Chem. Phys.,
1128 18(23), 17615–17635, doi:10.5194/acp-18-17615-2018, 2018.

1129 Ziska, F., Quack, B., Abrahamsson, K., Archer, S. D., Atlas, E., Bell, T., Butler, J. H.,
1130 Carpenter, L. J., Jones, C. E., Harris, N. R. P., Hepach, H., Heumann, K. G., Hughes, C.,
1131 Kuss, J., Krüger, K., Liss, P., Moore, R. M., Orlikowska, A., Raimund, S., Reeves, C. E.,
1132 Reifenhäuser, W., Robinson, A. D., Schall, C., Tanhua, T., Tegtmeier, S., Turner, S., Wang,
1133 L., Wallace, D., Williams, J., Yamamoto, H., Yvon-Lewis, S. and Yokouchi, Y.: Global sea-
1134 to-air flux climatology for bromoform, dibromomethane and methyl iodide, Atmos. Chem.
1135 Phys., 13(17), 8915–8934, doi:10.5194/acp-13-8915-2013, 2013.